Progress in Organic Coatings 210 (2026) 109646

Contents lists available at ScienceDirect

Progress in Organic Coatings

journal homepage: www.elsevier.com/locate/porgcoat

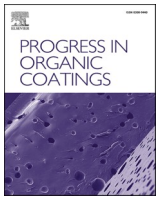

Evaluation of the corrosion protection of organic-coated zinc-alloy galvanised steels using novel, environmentally-friendly corrosion inhibitor pigments☆

Gwynfor Callaghan [a,*], Sonny Ngo [b], Geraint Williams [a]

[a] Department of Materials Science and Engineering, Swansea University, Bay Campus, Crymlyn Burrows, Swansea SA1 8EN, UK
[b] Beckers industrial Coatings, Goodlass Road, Speke, Liverpool L24 9HJ, UK

ARTICLE INFO

Keywords:
Galvanised steel
Cathodic disbondment
Filiform corrosion
Corrosion inhibitive pigments
Scanning vibrational electrode technique
ZMA

ABSTRACT

The corrosion behaviour of steel coated with either: a primarily zinc coating comprised of 0.15 wt% Al (HDG) or a zinc-aluminium-magnesium coating, 1.6 wt% Mg, 1.6 wt% Al, and 96.8 wt% Zn (ZAM) are investigated in the presence of industry standard and emerging, environmentally-friendly corrosion inhibitor technologies. With this paper evaluating the inhibitory performance of a functionalised oxy-amino-phosphate-salt of magnesium (OPMG), a hydrotalcite carbonate clay loaded with 4-aminobenzoic acid (HT-PABA), a calcium ion exchange pigment (Ca-Ex), and an inhibitor based on 2-(1,3-benzothiazol-2-ylithio) succinic acid (BTSA) dispersed in model poly-vinyl-butyral (PVB) coatings and 3.5 wt% NaCl (aq) solutions. With their inhibitory performance evaluated against two corrosion-driven coating failure mechanisms: cathodic disbondment (CD), and filiform corrosion (FFC) as a function of inhibitor loading. In the case of CD, an inhibitor ranking order of BTSA > HT-PABA > OPMG > Ca-Ex is observed, while OPMG and HT-PABA are the most effective at slowing rates of FFC. Potentiodynamic and scanning vibrating electrode (SVET) experiments were conducted to evaluate the efficiency of the most promising inhibitors at slowing rates of corrosion on the bare ZAM alloy surface and the exposed cut edges immersed in chloride solutions. With OPMG and BTSA both shown to act as net anodic inhibitors, resulting in an increase in the polarisation resistance by over an order of magnitude. Both inhibitors produced a derived 67 % reduction in total (zinc) metal loss at the exposed ZAM cut-edges over a 24 h immersion period against the control.

1. Introduction

Steels used for roofing and façades within the construction industry, are typically coated with zinc sacrificial coatings that cathodically protect the underlying steel as well as being further subjected to a coil coating process [1]. The coil coating process consists of an initial alkaline cleaning regime (pH ~ 10–11), the application of a subsequent inorganic chemical pretreatment layer, an organic composited primer (polymeric binder and corrosion inhibitive filler) and lastly a functionalised organic topcoat that provides an adherent, durable and corrosion resistant barrier [2]. However, during their service life the underlying metallic substrate can become exposed to corrosive electrolytes through penetrative coating defects or at the cut edges, that in turn can result in the initiation of corrosion-driven coating failure mechanisms, which damage the integrity of the coated steel [3]. Therefore, it is necessary to optimise the performance of the corrosion inhibitive materials within the chemical pre-treatment or primer layers to extend the service life of the coated products [4,5].

A previously widely used inhibitor that was shown to effectively inhibit several corrosion driven coating failure mechanisms was hexavalent chromium (CrVI) based technologies [6]. In recent years they have been banned from industry, or severely restricted due to their carcinogenicity and toxicity that pose significant health and environmental risks [7]. Therefore, the development of alternative environmentally friendly and sustainable inhibitor technologies is a current focus within the industry and will make up the key focus of this work. In addition, there is a need to investigate the comparative inhibitive performance of alternative inhibitors against several different corrosion

☆ This article is part of a Special issue entitled: 'ACPOC2024' published in Progress in Organic Coatings.

* Corresponding author.
E-mail address: 906414@swansea.ac.uk (G. Callaghan).

https://doi.org/10.1016/j.porgcoat.2025.109646
Received 2 May 2025; Received in revised form 31 August 2025; Accepted 1 September 2025

driven coating failure mechanisms that encompass traditional organically coated primary zinc (0.15 wt% Al) coatings as well as mechanisms seen only on zinc aluminium magnesium alloys coatings.

Zinc-Aluminium-Magnesium (ZAM) coatings have previously been shown to inhibit corrosion induced mass loss by two to three times when compared to primary zinc (HDG) coated steels (comparative coating thicknesses) [8,9]. The magnesium additions result in the formation of $MgZn_2$ intermetallics that undergo preferential anodic dissolution over the primary zinc and aluminium containing phases. The preferential dissolution results in the promotion of $Mg(OH)_2$ at the ZAM surface. The presence of $Mg(OH)_2$ has previously been shown to reduce the rate of the cathodic oxygen reduction reaction (ORR) as well as buffer the local surface pH to mildly alkaline conditions (10.5) where protective hydrozincite ($Zn_5(CO_3)_2(OH)_6$) and simonkolleite ($Zn_5(OH)_8Cl_2{\cdot}(H_2O)$) formation is favourable [9–11]. Moreover, at these increased pH values the aluminium containing phases are predicted to be anodically active releasing aluminates that in turn can react with Mg^{2+} cations to form protective layered double hydroxides (LDH) [9–11].

The two corrosion driven coating failure mechanisms utilised within this work include cathodic disbondment (CD) for organically coated HDG, and filiform corrosion (FFC) for ZAM (1.6 wt% Al, 1.6 wt% Mg) coated steels. CD has been shown to affect a range of organically coated metallic substrates including steel [12–17] and HDG [18–20] in the presence of penetrative coating defects and aggressive chloride electrolytes that results in the ingress of a thin alkaline electrolyte layer underneath the delaminated organic coating. This acts to couple the localised anodic metal dissolution reaction at the penetrative defect site to the mobile cathodic (ORR) that occurs at the delamination front [13,15]. The elevated alkalinity as well as the free radial intermediates that form during the ORR result in the degradation of the interfacial coating/metallic bonds, that lead to the progressive delamination of the organic coating [3,14,20–22]. The Mg-Zn and Mg-Al-Zn eutectic phases present within ZAM coatings has previously been shown to provide ZAM an intrinsic resistance to CD that has been attributed to an observed inversion in the electrochemical potential between the anodically active defect sites and the intact organically coated $MgZn_2$ phases. Moreover, the predicted low cathodic ORR activity of the eutectic phases renders the principle O_2 reduction cathode (on the primary zinc) discontinuous within the microstructure and thus inhibits the progression of the CD front past the defect site [9,23].

FFC occurring on organically coated iron, aluminium, magnesium and ZAM substrates initiated using a range of ‘contaminant’ containing electrolytes such as (iron/group 1) chlorides, sulphates, HCl and acetic acid (HAc) at high relative humidities has been studied (60–96 % RH) [24–29]. The process is characterised by the formation of mobile insoluble corrosion product filled ‘threadlike’ filaments that propagate from penetrative defects, that result in the anodic undercutting, and the resultant detachment of the organic coating at the electrolyte filled filament ‘heads’ [24–28].

FFC typically evolves through a two stage mechanism: the initiation stage where the electrolyte filled filament heads are formed at the defect coating boundary, and the propagation stage where filaments linearly propagate from the defect site driven by a differential aeration mechanism [28–31]. At the filament heads, an oxygen/potential gradient forms between the cathodic dominant alkaline (pH ~10) rear portion of the head and the anodic front. This is because oxygen availability being higher at the rear portion of the head due to the facile O_2 pathway through the porous corrosion product tail. Meanwhile oxygen solubility is limited at the front due to local high ionic strength and low pH (~1–5) generated by the anodic metal dissolution reaction [28–32].

The mechanism on coated ZAM firstly involves the preferential anodic dissolution of intermetallic $MgZn_2$ phases at the defect site that in turn allows O_2 to percolate to the underlying steel and allows cathodic ORR at the rear portion of the head. Deposits of insoluble hydroxide based corrosion products then precipitate underneath the organic coating in the wake of the mobile filaments as they propagate from the defect site [31]. FFC on coated ZAM has previously been shown to differ to other coated substrates. It only repeatably initiates in the presence of Hac and is attributed to the dissolution of the $MgZn_2$ intermetallic phases producing O_2 pathways to the steel [26]. Another difference is that during the propagation of filaments during FFC on ZAM several filaments are capable of crossing over one another, which is at odds with the mechanism on coated iron where separate filaments are deflected from one another [30,32]. This inability to cross over has been attributed to the limited presence of water soluble components within the tail regions of existing active filaments as well as the fact that if another filament were to crossover it would encounter another source of O_2 leading to the disruption of the local positions of differential aeration cell sites [32]. These differences highlight that firstly sufficient Mg rich phases must remain within the tail regions to maintain the required anodic activity for the crossing filament to propagate as well as that the cathodic activity of crossing filaments are not interrupted by the new source of O_2 during FFC on ZAM [32]. Moreover, the ability for filaments to cross over one another suggests that the corrosion product deposits formed within the tail regions are insufficient barriers to prevent the further anodic dissolution of the corroded ZAM surface [32].

Anti corrosion inhibitors formulated into either the chemical pretreatment or organic primer layer have previously been shown to inhibit both the initiation and rate progression of both CD and FFC on HDG and ZAM substrates respectively. Inhibitor pigments release ionic species into the electrolyte that alter the local electrolytic conditions around defects and modify the corrosion products that form [2,4,16,17,29]. While the research surrounding the inhibition of CD on HDG substrates is extensive there has been limited work surrounding the inhibition of FFC on ZAM coated substrates with the use of fully commercialised organic primer formulations. This work aims to expand on the current literature related to inhibitors technologies that are effective against both CD and FFC on zinc and zinc alloy coated steels [31,32].

One inhibitor technology that shows promise is based on ion exchangeable hydrotalcite (HT) functionalised anionic clays formed of layered lamellar mixed hydroxides (LDH), with the work focussing on LDH based on double layered aluminium magnesium hydrotalcite [20,32].Within the HT pigment structure, the trivalent Al^{3+} ions present in the octahedral positions are randomly substituted for Mg^{2+} ions that result in the specific layer exhibiting a net positive charge. The electroneutrality is then maintained by exchangeable anions that locate themselves within the interlayer spaces between the layered structures [33]. Where Eq. (1) shows the general formula for an anionic clay where M^{2+} and M^{3+} are the divalent and trivalent metal ions respectively, A^{n-} is the interlayer exchangeable anion.

$$\left[M^{2+}_{1-x}M^{3+}_{x}(OH)_2\right]^{x+}\left[A^{n-}_{\frac{x}{n}}yH_2O\right] \quad (1)$$

Natural or synthetic HT pigments have previously been shown to inhibit a range of corrosion driven mechanisms through exchanging out aggressive anions from aqueous solutions for either carbonate (natural found interlayer anion) or other intercalated anti-corrosive anionic species [20,32]. With the HT pigment able to actively inhibit corrosion through a controlled release mechanism resulting in the progressive removal of Cl^- or acetate anions (Ac) from the electrolyte or filament heads (for FFC) as well as the progressive neutralisation of the solution or low pH present within filament heads [20,32].

Organic based inhibitors are a class of inhibitors that have been investigated in detail and could provide an efficient, environmentally friendly alternative to hexavalent chromium [34–39]. Where the inhibitors are classified by the presence of either inorganic (nitrates, phosphates, chromates) or organic (amino acids, alcohols, carboxylic acids and amines) compounds [35]. The inhibitors work by either forming protective salt films or adsorbing onto the metal surface leading to the passivation of the surface [35,38–52]. With organic compounds that contain heteroatoms (N, O, S) and electron rich centres formed through polar substituted organic compounds (hydroxyl, methoxy,

amines, nitrile, and carboxylic acid groups) being shown to act as efficient corrosion inhibitors even in the presence of chloride rich and extreme pH environments [49–53].

One such class of inorganic inhibitors that has been utilised heavily within industry as direct replacements to hexavalent chromium is phosphate based pigments consisting of phosphate anions combined with either zinc, calcium, aluminium, and magnesium cations [5,54–57]. Sparingly soluble phosphate based pigments released from organic coatings act to inhibit corrosion through either passivating the exposed metallic substrate, forming mixed phosphate metal films and buffering the local pH within the electrolyte [53–57]. The precipitated film inhibits the diffusion of aggressive species in the electrolyte during CD and FFC effectively inhibiting both the initiation and propagation stages for CD and FFC [5,20,54–57].

This work seeks to systematically investigate the inhibition performance of a range of emerging environmentally friendly corrosion inhibitor technologies that include: a HT based pigment (HT-PABA) containing both carbonate and 4-amino benzoic acid interlayer anionic species, an inhibitor based on 2-(1,3-benzothiazol-2-ylithio)-succinic acid (BTSA), and an oxy-amino-phosphate-salt of magnesium (OPMG). The pigments are formulated into model poly-vinyl-butyral co-vinyl co-acetate (PVB) coatings to evaluate and compare their inhibitory performance against CD, and FFC on HDG and ZAM coated steels respectively. Following this initial investigation, electrochemical testing (potentiodynamic and linear polarisation testing (LPR)) is used to investigate the inhibitors anti-corrosion performance for bare (uncoated) ZAM substrates through direct inhibitor additions into 3.5 wt% $NaCl_{(aq)}$ electrolytes. Lastly a scanning vibrating electrode technique (SVET) is used to measure and map the anodic and cathodic surface activity for immersed ZAM cut edge samples in the presence of the inhibited 3.5 wt% $NaCl_{(aq)}$ electrolytes and report semi-quantative mass losses over the 24 h experiment. An industry standard silica based calcium exchange pigment (Ca-Ex) used as a secondary control to compare the inhibition performance of the screened inhibitor technologies against a readily adopted inhibitor technology [22].

2. Materials and methods

2.1. Metallic specimens

Zinc coated steel samples were provided by Tata steel UK and consisted of 0.7 mm gauge mild steel coated with either a predominately zinc (HDG) or zinc-aluminium-magnesium (ZAM) metallic coating applied either of the steel. With the HDG coating comprising of ~99.85 wt% zinc, and 0.2 wt% aluminium and the ZAM coating consisting of 1.6 wt% additions of aluminium and magnesium at a 1:1 ratio to the zinc galvanising chemistry. With the coatings applied at 20 μm (10 μm either side of the steel) as was confirmed through optical characterisation of the cut edges respectively. Samples were cut into either 5 × 5 cm or 2 × 2 cm coupons for the corrosion driven coating failure testing or potential-dynamic testing, respectively.

2.2. Pigments/chemical reagents

All inhibitor pigments, chemicals and reagents used were of analytical or commercial grade purity with the Polyvinyl butyral-*co*-vinyl alcohol-co-vinyl acetate (PVB) Mw 70,000–100,000, acetic acid (HAc), solvents and cold mounting resin used were obtained from Sigma Aldrich Chemical Co and MetPrep Ltd. The inhibitor technologies evaluated within this work were of commercial grade and currently being used within the coating industry on coated HDG systems.

2.3. PVB model coating loading

Model coatings were formulated with the various inhibitor pigments through dispersing the pigments within the 15.5 % w/w PVB coatings according to Eq. (2), with pigments that were fully soluble in the ethanol solvent (BTSA) dispersed based on total wt% additions [19,20,28]. Where PVF represents the pigment volume fraction, M_{PVB} and ρ_{PVB} are the mass and density (0.8 g cm^{-1}) of PVB, respectively, and $M_{pigment}$ and $p_{pigment}$ are the mass and density of the pigments introduced ($g{\cdot}cm^{-1}$).

$$PVF = \left(\frac{1 + M_{pvb-\rho_{pigment}}}{M_{pigment} \cdot \rho_{PVB}}\right)^{-1} \quad (2)$$

2.4. Metallographic preparation

ZAM and HDG samples prior to coating with the model PVB coatings were first polished using a 5 μm alumina slurry to remove the resultant oxide layer (~2 μm) to form a uniform and consistent surface. Specimens were then rinsed with distilled water and either ethanol or hexane/ethanol (ZAM specimens) to remove contaminants generated during the galvanising process followed by air drying [3,20,31]. ZAM samples used for the potential dynamic testing were polished using 1 μm aqueous diamond polishing solution and then rinsed using the first solution stated above. Lastly, ZAM samples used during the SVET testing were initially cold mounted in a non-conductive epoxy based resin only exposing the cut edge to the solution and then were mechanically ground with silicon carbide abrasive paper grades #400–1200 followed by polishing with a 1 μm water based diamond suspension to achieve a smooth surface free of surface artefacts as required during the SVET testing.

2.5. Model coating corrosion cells

The model coatings used were bar cast across the zinc coating surfaces using a glass rod to form 30 μm dry film thickness (DF) coatings after air curing using parallel strips of PVC tape as height guides. The specific cell setup was dependent on the coating failure mechanism being investigated where Fig. 1 summarises the coating/defect generation procedure for both CD and FFC.

For the case of CD, a strip of thin static free adhesive tape is laid down adjacent to one of the substrate edges covering 1.5 cm of the metal surface followed by two parallel strips of 120 μm thick PVC tape laid down at right angles to the adhesive tape, leaving a 2 cm wide strip of the bare metal within the centre of the coupon.

The model PVB coatings are then bar cast over the sample and left to air dry for 30 min prior to introducing the artificial coating defect as described by Stratmann et al. through cutting a section of the thin adhesive tape and lifting the residual lip [12–14]. Lastly non-corrosive silicon sealant was added to form the electrolyte well around the artificial coating defect and left to cure for 24 h. The samples were then initiated by adding a 5 wt% $NaCl_{(aq)}$ pH solution to the electrolyte well and placed in a humidity controlled chamber maintained at a Relative humidity of 96 % using a reservoir of 5 wt% NaCl. A continuous time-lapse method was implemented to measure the delamination distance from the artificial defect against time by monitoring the progression of the electrolyte ingress underneath the transparent PVB coatings with images taken every 5 min up to 1 week and then processed using image analysis software (ImageJ).

In the case of FFC the same method is used to generate the 30 μm DF PVB coatings but without the artificial coating delamination feature. Instead, two parallel 1 cm penetrative defects are introduced through the coatings by scribing down to either the zinc substrate or the steel using a surgical scalpel. With the defects introduced down to either the steel or ZAM through varying the applied force when scribing down with this method concurrent with previously established methods [31]. However, due to the thin zinc coatings a small region of iron could be exposed even within the ZAM scribes, but a larger proportion of exposed iron would still be expected for the scribes made down to the steel based on previous testing and optical characterisation. Coated ZAM samples were then initiated through the addition of 2 μL of 1.5 M HAc (pH ~2–3)

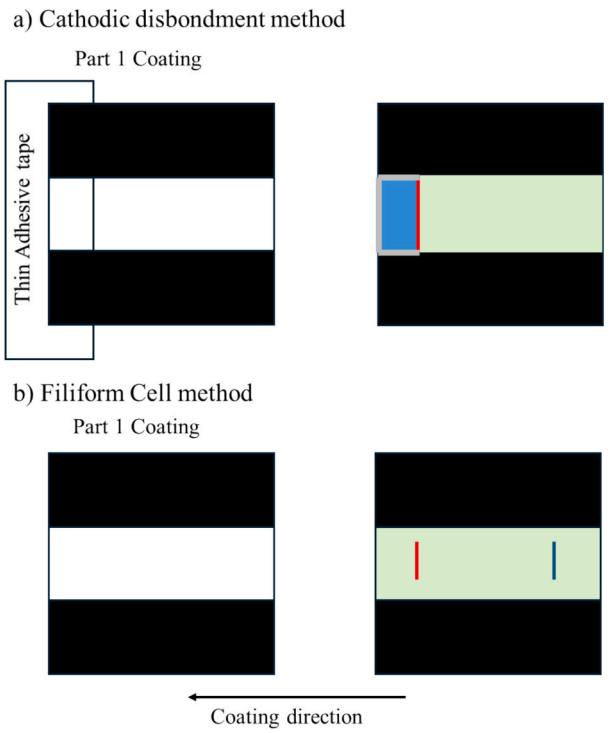

Fig. 1. Schematic of the corrosion driven coating failure test cell methodologies including the PVB coating (part 1) and defect formation (part 2) with the green area representing the coated surfaces. For the formation of the CD cell (a.) an artificial coating defect (red line) and electrolyte well (blue region) are formed. The Filiform corrosion cells (b).consist of two penetrative scribe defects where the vertical lines represent the defects formed down to the ZAM (red) and the steel (black). (For interpretation of the references to color in this figure legend, the reader is referred to the web version of this article.)

to each scribe. The coated samples were then placed in a sealed humidity controlled chamber maintained at a RH of 93 % using reservoirs of saturated $Na_2SO_4{\cdot}10H_2O$ [3,28,31]. Images were then taken weekly up to 7 weeks and processed using image analysis software (ImageJ) to measure and quantify the extent of filiform corrosion originating from each scribe. With the samples removed from the chamber weekly to take the images as well as refresh the air within the chamber. A pre-measured real distance between two points was used to calibrate the software with the total corroded scribe area measured for 3 scribes per inhibitor loading and classification of scribe (ZAM or steel layer to determine an average total corroded scribe area with the error corresponding to one standard deviation from the mean measured area.

2.6. Electrochemical polarisation testing

Potentiodynamic and LPR measurements were conducted using a Gamry interface 1010 potentiostat in combination with a 3-electrode arrangement comprising a saturated calomel reference electrode (SCE), platinum foil counter electrode, and a 0.36 cm^2 square exposed area of the ZAM coupon as the working electrode. All electrochemical testing was conducted in 3.5 wt% NaCl $_{(aq)}$ solutions with direct inhibitor additions, with the pH of the solutions adjusted using 2 M HCl and 1 M NaOH to a pH of 7 to allow direct comparisons between the inhibitors tested (variable solubility at different pH values). Samples were immersed within the electrolytes and left at OCP for 5 min to stabilise prior to polarisation with potentiodynamic scans initiated at 150 mV either side of the open circuit potential (OCP) and polarised to 0.3 V either side of the OCP vs SCE at a scan rate of 0.166 Vs^{-1} to generate the anodic and cathodic sweeps during testing. The anodic and cathodic sweeps were measured independently on fresh samples and electrolytes with the averaged data from three repeats merged for analysis. LPR testing was conducted by polarising the samples ±15 mV from the OCP at the same scan rate with the corresponding current density measurements taken hourly up to 12 h for each experiment. With the polarisation resistance (R_p) value per scan calculated from the slope of the resultant potential vs. current density plots around the corrosion potential (E_{corr}). The corrosion current (i_{corr}) determined from the Stearn-Geary relationship seen in Eq. (3) where B is the Stearn-Geary coefficient shows that the R_p values are inversely proportional to i_{corr} and therefore a higher R_p corresponds to a lower corrosion rate. Where the value of B itself is determined from the anodic (β_a) and cathodic (β_c) Tafel slopes as seen in Eq. (4). Therefore, by plotting the R_p values generated against time the inhibition performance of the electrolytes can be characterised against time.

$$i_{corr} = \frac{B}{R_p} \tag{3}$$

$$B = \frac{\beta a\, \beta c}{2.303\,(\beta a + \beta c)} \tag{4}$$

2.7. SVET methodology

The polished and cold mounted cut-edge samples were masked using PTFE tape to expose a fixed 6 × 6 cm area to the electrolyte and fastened at the bottom of a glass dish with the electrolyte added prior to initiating the scan but after the height scanning was taken to map the scan area with a schematic of the SVET coupons shown in Fig. 2. The exposed cut edges were masked to ensure that the area selected was free from artificial defects and had a uniform zinc coating either side of the steel. The scan area was set to a 3 × 6 mm rectangular area (taken in the x and y directions respectively) at a 100 μm resolution (31 × 61 total data points) to completely scan over the exposed cut edge within the masked area. With one scan taken every hour up to 24 h with three repeat tests taken per electrolyte solution to calculate average derived zinc metal losses and inhibitor efficiency values.

For all SVET cut-edge experiments 3.5 wt% pH 7 NaCl $_{(aq)}$ solutions with direct inhibitor additions as described before in Section 2.6 were used with the dissolved oxygen concentration within the bulk electrolytes presumed to be equal to the value for air-saturated water (2.8×10^{-4} mol dm^{-3}) [58]. The SVET measurements were performed using an in-house developed SVET setup using a micro-tip probe consisting of a 125 μm diameter platinum wire enclosed in a glass sheath. With the probe vibrating perpendicularly at a constant frequency of 140 Hz and an amplitude of 25 μm at a fixed 100 μm height above the corroding surface. Where detailed descriptions of the operation and calibration procedures can be found in detail in previous literature which also include the 3D height scanning taken prior to scanning to ensure a

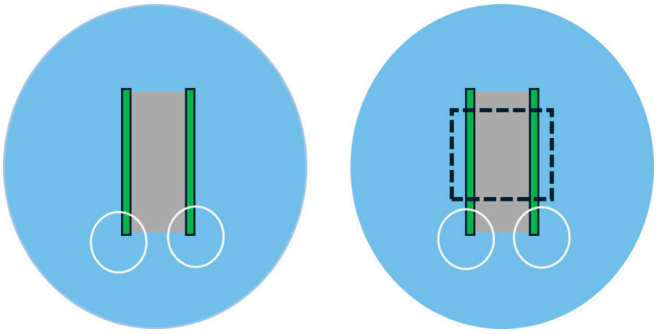

Fig. 2. Schematic of SVET ZAM cut edge samples With the exposed ZAM coatings (green) and the exposed steel(grey) enclosed in a fixed exposed area through masking with PTFE tape (exposed area within the dotted square). (For interpretation of the references to color in this figure legend, the reader is referred to the web version of this article.)

consistent scan height above the exposed cut edge [59].

In simplified terms during the corrosion process potential fields establish within the electrolyte due to the movement of the ionic current flux between the anodic and cathodic sites that develop. As the vibrating probe intersects these fluxes an alternative potential is recorded that is proportional to potential gradient in the direction of the vibration. Where the measured alternative potential is directly proportional to the ionic current flux which in turn provides a means of spatially and temporarily resolving the anodic and cathodic features that develop across the cut-edge along with their associated intensity during the scan. Furthermore, the SVET testing provides a semi-quantitative method to measure the metal loss during the experiment through an integration of the total measured anodic current (i_a) through an application of Faraday's law where the measured SVET potentials (V) are converted to current density (j_z (Am^{-2}) values through multiplying them by the calibration factor generated prior to the scanning. The total i_a value is generated through the integration in Eq. (5) where x and y represent the length and width of the scan area.

$$i = \iint_{0\,0}^{x\,y} j_z(x,y)dxdy \tag{5}$$

With the resultant mass loss per scan then calculated using Eq. (6) that incorporates Faraday's constant (F 96487 $Cmol^{-1}$), charge (Q), the number of electrons (2 for Zn) and the atomic weight of zinc (A_r). With the total experimental mass loss calculated by summing the mass losses calculated per individual scan throughout the experiment.

$$Mass\ loss\ (m) = \frac{Q}{n.F}A_r \tag{6}$$

Several assumptions are made during the analysis including that a constant corrosion rate occurs in between scans, that only zinc is considered during the mass loss calculations, and that the individual anodic and cathodic sites that develop are separated by at least ~150 μm due to the limitations of the SVET measurement resolution [59–61].

Thus, despite these limitations the SVET derived mass losses have previously been shown to be comparable to those obtained from external Zn runoff tests and therefore can be used as a tool to deduce the anti-corrosion performance and mechanistic information for the inhibition of immersed metallic specimens in the presence of anti-corrosive species and aggressive electrolytes [62].

3. Results and discussion

3.1. Cathodic disbondment study

Following the method outlined in Section 2.5, an initial screening exercise was conducted to systematically investigate the CD kinetics for the pigmented PVB coated HDG substrates at 0.1 PVF or 3 wt% (BTSA) inhibitor loadings against the control uninhibited PVB coated HDG, with the extrapolated delamination distances plotted against time and summarised in Fig. 3.

Where the kinetics of CD for the control PVB coatings on HDG having been previously comprehensively studied through timelapse and in-situ scanning kelvin probe (SKP) techniques [3,19,20]. Fig. 4 shows representative visual timelapse images of the CD process for the control coated HDG specimens with the first image (left) showing the sample immediately after initiation followed by images showing the ingress of the electrolyte (darkened region) underneath the intact coating past the defect boundary (red line). The delamination distance (x_{del}) corresponds to the average linear distance measured between the red horizontal line and the electrolyte front taken at corresponding time (t_{del}). With the observed time taken for the electrolyte to first ingress past the coating defect site (second image Fig. 4) denoted as t_i and is representative of the time taken for the galvanic cell to establish (initiation time).

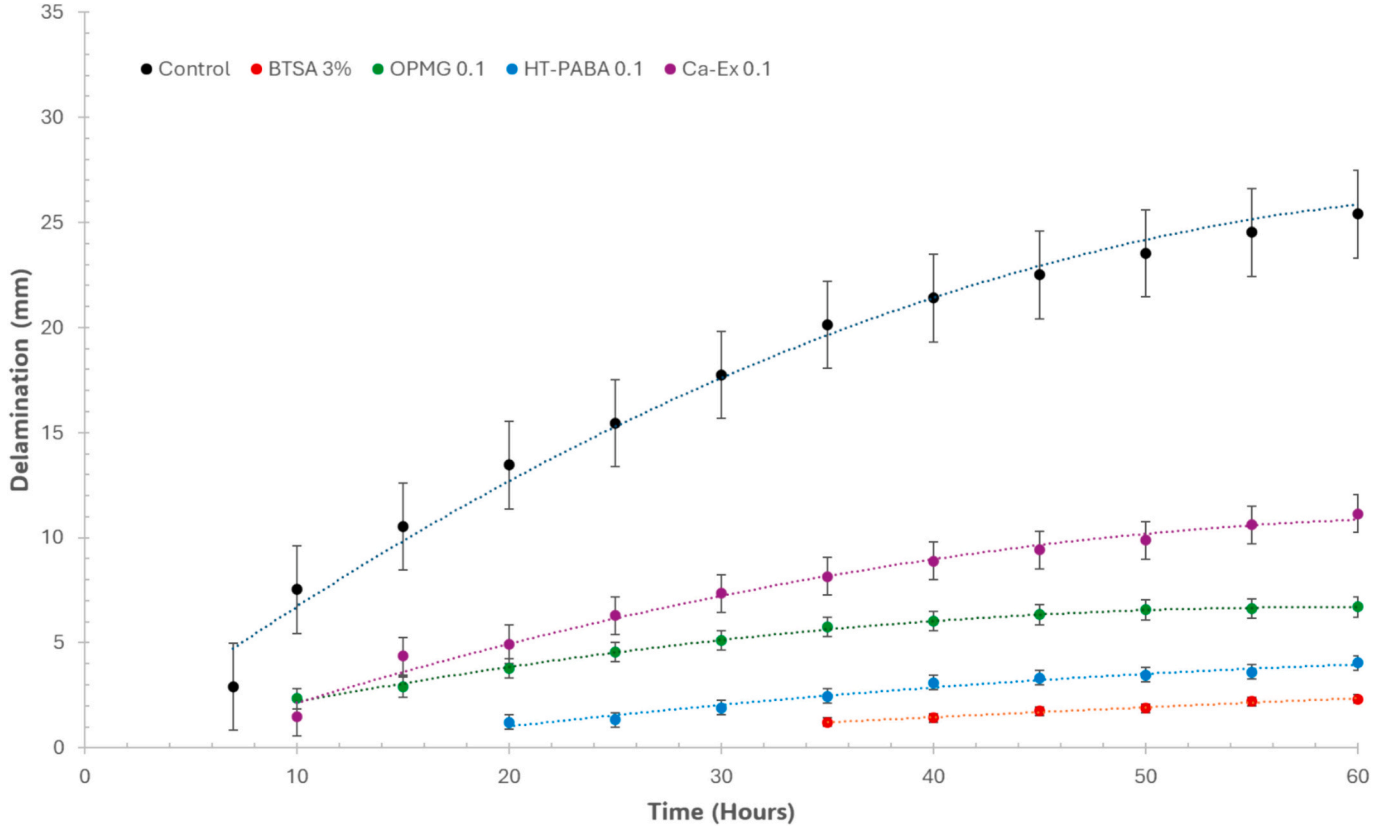

Fig. 3. Time dependent delamination distances (x_{del}) plots for the Unpigmented (Control) and inhibited model PVB coatings on HDG at inhibitor loadings of 0.1PVF or 3 wt% initiated using 5 wt% pH 7 $NaCl_{(aq)}$ solutions. Error measurements correspond to ± one standard deviation from the average from 3 repeat experiments.

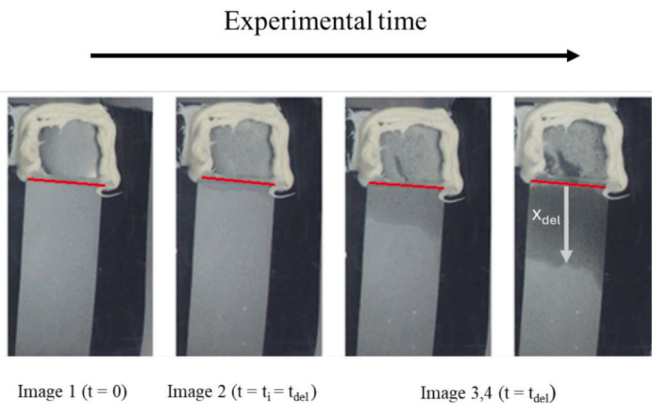

Fig. 4. Visual representative timelapse images during Cathodic disbondment (CD) for the model PVB coatings on HDG initiated using 5 wt% ~ pH 7 NaCl $_{(aq)}$ solutions. Where the red line represents the defect/coating boundary, the grey line represents the delamination distance (x_{del}). (For interpretation of the references to color in this figure legend, the reader is referred to the web version of this article.)

Once the control PVB coated HDG sample is initiated with the chloride containing electrolyte, the exposed zinc surface within the defect site begins to corrode, that in turn results in the development of a potential difference between the anodic defect site and the intact coating region [63,64]. The potential difference generated drives metal cations to migrate to the intact coating interface, which in turn results in a drop in the local potential leading to the initiation of the cathodic ORR at the defect/coating boundary and the resultant detachment of the intact coating. The resultant galvanic cell that forms couples between the mobile local cathode at the delamination front and the localised anode within the electrolyte well through the ionic current that passes through the thin electrolyte film that ingresses underneath the delaminated coating. Electrons required for the cathodic ORR (Eq. (7)) are provided by the metal dissolution reaction (Eq. (8)) within the defect site; with oxygen and water freely available at the intact coating interface through diffusion from the humid environment (96 % rh.) via the bulk polymer coating as the delamination front progresses past the defect site [63,64].

$$O_2 + 2H_2O + 4e^- \rightarrow 4OH^- \quad (7)$$

$$Zn_{(s)} \rightarrow Zn^{2+} + 2e^- \quad (8)$$

Several mechanisms exists for the resultant detachment of the organic coating during CD for coated HDG substrates and include: the dissolution of amphoteric zinc oxide at the substrate/coating boundary; localised attack of the polymer via alkaline hydrolysis; the physical displacement of the coating through the formation of a high pH aqueous film; and lastly that the intermediate products generated during the ORR such as peroxide ions (HO^{2-}) superoxide radicals (O^{2-}) and hydroxyl radicals ($^{\cdot}OH$) attack the coating leading to the disbondment at the coating/metal interface [3,14,20–22,65,66]. The first disbondment mechanism involves the dissolution of the amphoteric zinc (hydr)oxides present at the substrate/coating boundary through the increase in the local underfilm alkalinity generated by Eq. (7), that results in the disbondment of the coating and the formation of soluble aqueous bizincate ($HZnO_2^-$) zincate (ZnO_2^-) species according to Eqs. (9) and (10) [1,22,23].

$$Zn(OH)_{2\ (s)} \leftrightarrow HZnO_{2\ (aq)}^- + 2H_{(aq)}^+ \quad (9)$$

$$Zn(OH)_{2\ (s)} \leftrightarrow ZnO_{2\ (aq)}^{2-} + 2H_{(aq)}^+ \quad (10)$$

Another mechanism closely related involves the detachment of the polymer via direct alkaline hydrolysis of the metal/coating interfacial bonds. However, the likelihood of this mechanism playing a significant part in the coating detachment has been contested through a previous study where an immersed coated metal with an artificial defect in a strong sodium hydroxide solution resulted in no disbondment [67]. Which further suggests that the direct hydroxyl attack of the polymer does not in fact play an extensive role in CD and that in fact the two mechanisms could potentially hold more relevance to the initiation stage of CD on coated HDG substrates rather than the delamination of the polymer. The last mechanism where free radicals (HO^{2-}, O^{2-} and $^{\cdot}OH$) generated at the delamination front through the ORR attack the interfacial coating/metal bonds has been shown to be more detrimental to the resultant coating disbondment which is further supported by the previous study and is taken as the more widely adopted mechanism [3,19,20,65,66].

Fig. 3 clearly shows the efficiencies of the inhibitors in question regarding their ability to inhibit the rate of delamination once the galvanic cell establishes as well as the inhibition to t_i. With the control sample showing signs of coating delamination after 5 h, contrasting to the 10 h required for OPMG and the Ca-Ex loaded PVB coatings to initiate. HT-PABA and BTSA showed the greatest level of inhibition to t_i with both coatings only showing signs of delamination after 20 and 35 h from initiation, respectively.

With the rate limiting mechanisms for CD traditionally attributed to either the diffusion controlled mass transport of cations (Na^+) from the electrolyte well (artificial defect site) to the delamination front that gives rise to parabolic controlled delamination kinetics, or a linear controlled delamination signifying that the interfacial electron transfer associated with the cathodic ORR would be rate limiting [10,66–71].

However, recent literature has shown that the rate limiting mechanism of CD for model and commercial coated steels is in fact the cation (Na^+) insertion into the cation free interface, with observed linear or parabolic trends in coating delamination a direct result of the magnitude of the ohmic drop along the delaminated interface [63,64]. Where if this value is small, the potential drop across the delamination front (driving force for cation insertion) would remain constant, which in turn would result in a constant progress of the delamination front (linear controlled). With parabolic delamination kinetics a result of a high observed ohmic drop leading to the steady decrease of the potential drop across the front, and a steady decrease in the delamination rate [63,64]. With the same authors showcasing that the mechanism on different commercial polymers was unchanged (parabolic dependent cation insertion) with only the rates of delamination shifted between the coatings [63,64]. Furthermore, XPS analysis of the delaminated iron/polymer surfaces revealed that the cation concentration measured was independent of the experimental time and thus postulated that the role of hydroxyl ions generated at the delamination front was to migrate to the defect site to achieve charge neutrality and that Na^+ cations pull down the potential to enable the ORR and delamination to occur as seen in Fig. 5 [64,65].

Therefore, to firstly deduce if linear or parabolic delamination kinetics had occurred the extrapolated x_{del} values from Fig. 3 were plotted against the square root of t_{del} minus t_i. With the linear relationships seen in the resultant plots (Fig. 6) indicative of parabolic delamination kinetics for both the control and inhibitive model coatings, with the gradient of the plots equal to the delamination rate constants (K_{del}) as seen in Eq. (11). The K_{del} values for the control and inhibited coatings were then used to calculate the inhibitor efficiencies against the rate progression of CD and summarised in Table 1. The primary source of error when determining K_{del} is the accurate determination of the average delamination front from the timelapse images due to the discontinuous delamination front. Therefore, the standard deviation from three repeat measurements of K_{del} for each coating iteration was included within Table 1.

$$X_{del} = K_{del}(t_{del} - t_I)^{1/2} \quad (11)$$

Table 1 shows that BTSA, HT-PABA, OPMG and Ca-Ex additions

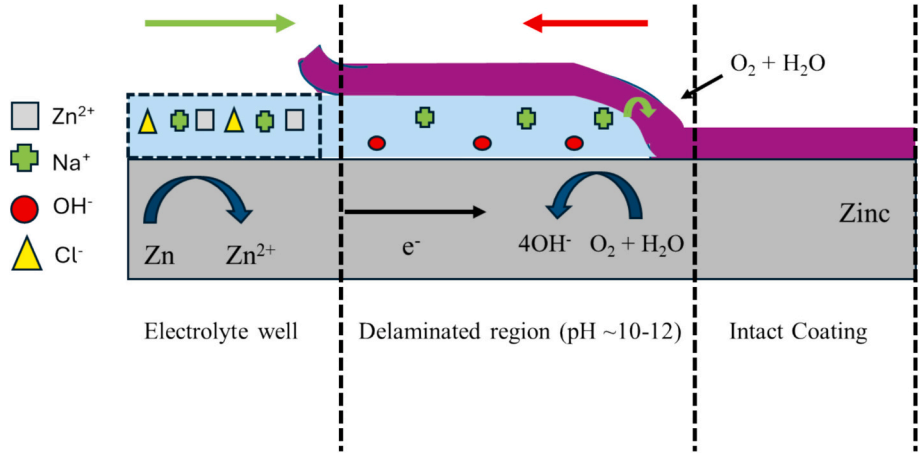

Fig. 5. Cross-sectional schematic for the CD mechanism on PVB coated HDG with initiated using 5 wt% pH 7 $NaCl_{(aq)}$ solutions. The cation insertion mechanism is shown by the green arrow at the delamination front. With the progression of the electrolyte underneath the intact coating occurring from left (defect site) to the right. (For interpretation of the references to color in this figure legend, the reader is referred to the web version of this article.)

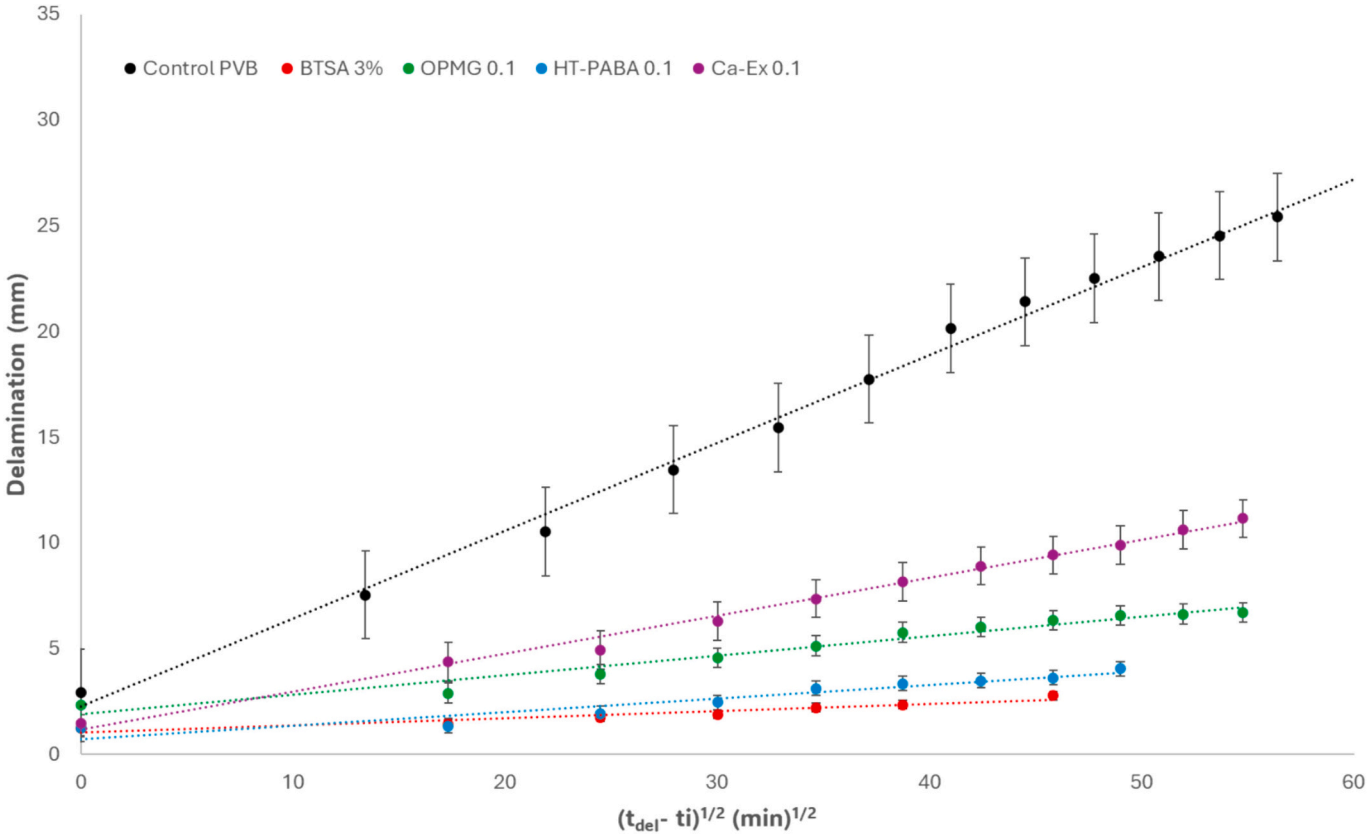

Fig. 6. Plots of delamination distance (x_{del}) as a function of $(t_{del}\text{-}t_i)^{1/2}$ for the control and inhibited PVB films containing 0.1 PVF or 3 wt% (BTSA) inhibitor additions after initiation with 5 wt. ~ pH 7 $NaCl_{(aq)}$ solutions $NaCl_{(aq)}$.

resulted in a reduction in the rates of disbondment as well as an increase in t_i compared with the control, with the specific order of inhibitors listed above corresponding to the ranking order of inhibitor efficiencies (highest to lowest), respectively. With BTSA, HT-PABA, and OPMG all resulting in a reduction of K_{del} by at least 78 % as well as a significant increase in the time taken for the delamination front to progress past the artificial defect boundary.

To further investigate the inhibitory performance of the most effective inhibitors as a function of inhibitor loading the model PVB coatings were formulated at inhibitor loadings of 0.025 to 0.1 PVF or 1–3 wt% (BTSA), with the resultant delamination square root rate plots shown in Fig. 7a–c and the extrapolated K_{del} and inhibitor efficiencies summarised in Table 2.

The secondary inhibitor screening clearly showed that by increasing the inhibitor additions within the PVB coatings an increased inhibition of the delamination rates as well as an increase in t_i is observed, where BTSA displayed a consistent increase in t_i through the increased pigment loadings as well as the highest inhibition to the rate kinetics of CD. While HT-PABA only showed a further inhibition to t_i past a loading of 0.05 PVF, with OPMG showing no change across the different loadings.

Table 1
Summary of the parabolic rate constants (K_{del}), inhibitor efficiencies (ΔK_{del} %) and time for delamination kinetics to establish (t_i) for the control and inhibited PVB coatings at 0.1PVF or 3 wt%. Errors correspond to ± one standard deviation from the mean measured K_{del} values from three repeat experiments.

	K_{del} (μm mins$^{1/2}$)	ΔK_{del} (%)	t_i (Hours)
PVB	413.0 ± 11.6	0 %	5
Ca Ex	179.7 ± 5.0	56 %	10
OPMG	92.5 ± 2.6	78 %	10
HT-PABA	63.5 ± 1.8	85 %	20
BTSA 3 %	33.6 ± 0.9	92 %	35

The inhibitor efficiencies for both BTSA and OPMG at inhibitor additions of 2 wt%. and 0.05 PVF respectively appeared to reach a threshold loading with both inhibitors showing minimal change to K_{del} at the higher inhibitor loadings. While HT-PABA showed a significant increase in inhibition past 0.025 PVF as a shift from 26 % to 66 % inhibitor efficiency was observed, with only a moderate comparative further increase seen at the 0.1 loading.

3.2. FFC results

The inhibition of FFC corrosion as a function of inhibitor loadings was systematically studied following the methodology outlined in Section 2.5, where the total corroded scribe area was measured weekly following initiation with 2 μL of 1.5 mol dm^{-3} HAc to either penetrative scribes formed down to the ZAM layer (Scribe 1) or Steel (Scribe 2). Where the rate kinetics for FFC on ZAM substrates are typically characterised by comparing the progression of the total corroded scribe area that develops around the defect sites due to constraints around distinguishing individual filaments at the later stages of FFC as well as the ability of filaments to crossover one another during the mechanism [59].

Fig. 8 shows representative images for the observed FFC on the ZAM substrates after seven weeks from initiation for the control and highest inhibitor (same loadings used for CD) loaded coatings. Following initiation all PVB coatings showed the formation of an initial corroded blistered region followed by the propagation of filaments after two weeks in perpendicular directions from the defect, with the position of the filament heads estimated by the darkened region at the end of the individual filaments. A greater total corroded scribe area was also observed for all coating systems when the scribe was formed down to the underlying steel, attributed to the larger more efficient iron cathodic area available for oxygen to freely percolate to and participate in the cathodic ORR.

Fig. 8 clearly shows that a greater initial blister area formed for the control coatings as well as a larger number of filaments that initiated and propagated from the scribe. With the Ca-Ex PVB coatings displaying a

Table 2
Summary of the parabolic rate constants (K_{del}), inhibitor efficiencies (ΔK_{del} %) and time for delamination kinetics to establish (t_i) for HT-PABA, OPMG, and BTSA PVB coatings loaded with either 0.025–0.1 PVF or 1–3 wt% respectively With errors corresponding to ± one standard deviation from the mean measured k_{del} values from 3 repeat experiments.

	K_{del} (μm mins$^{1/2}$)	Δ K_{del} (%)	t_i (Hours)
BTSA 1 %	114.9 ± 3.2	72	10
BTSA 2 %	43.8 ± 1.2	89	20
BTSA 3 %	33.6 ± 0.9	92	35
HT-PABA 0.025	296.7 ± 8.3	28	10
HT-PABA 0.05	139.4 ± 3.9	66	10
HT-PABA 0.1	63.5 ± 1.8	85	20
OPMG 0.025	196.7 ± 5.5	52	10
OPMG 0.05	120.2 ± 3.4	71	10
OPMG 0.1	92.5 ± 2.6	78	10

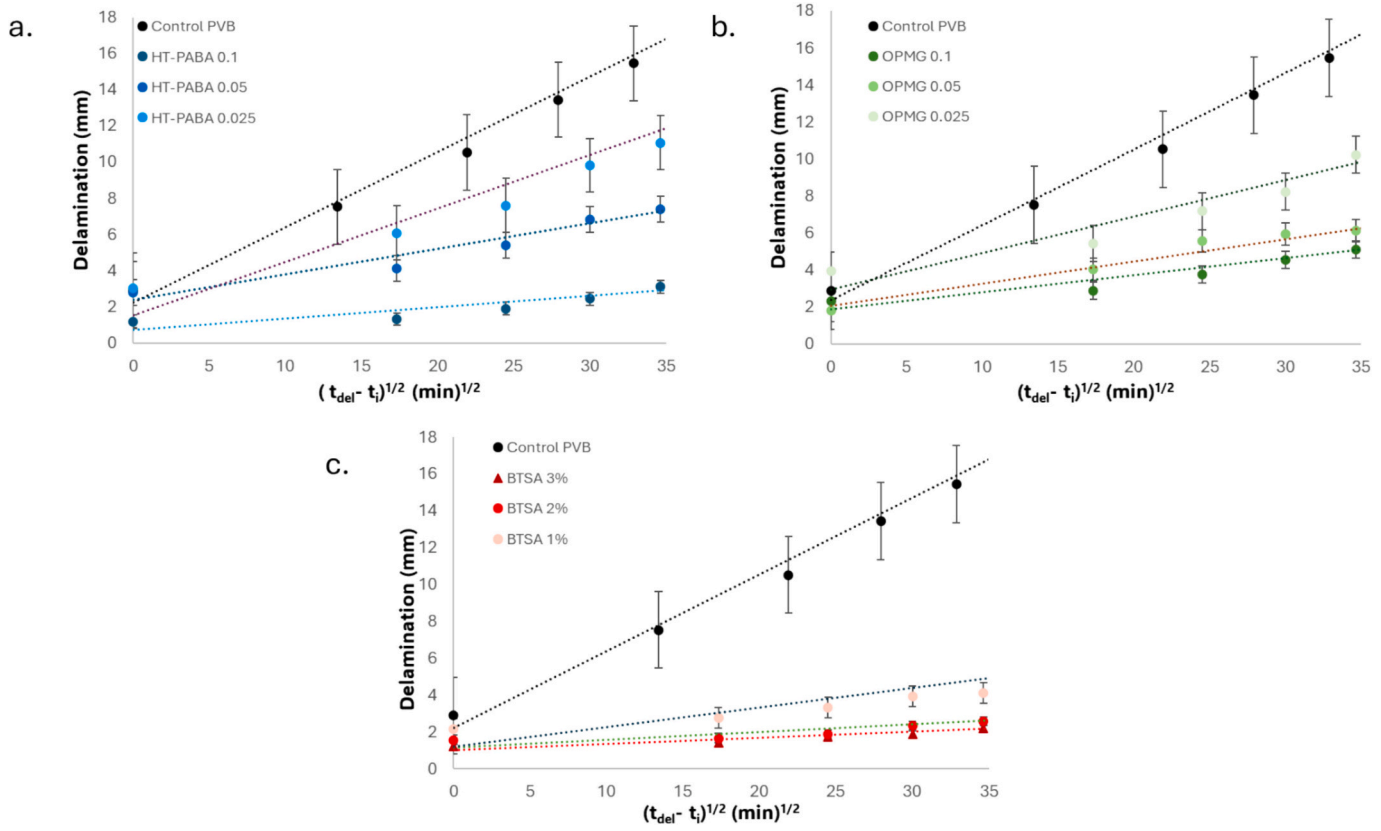

Fig. 7. Plots of delamination distance (x_{del}) as a function of $(t_{del}\text{-}t_i)^{1/2}$ for a) HT-PABA, b) OPMG, and c) BTSA PVB films containing inhibitor loadings from 0.025 to 0.1 PVF or 1–3 wt% respectively initiated using 5 wt% ~ pH 7 NaCl $_{(aq)}$ solutions.

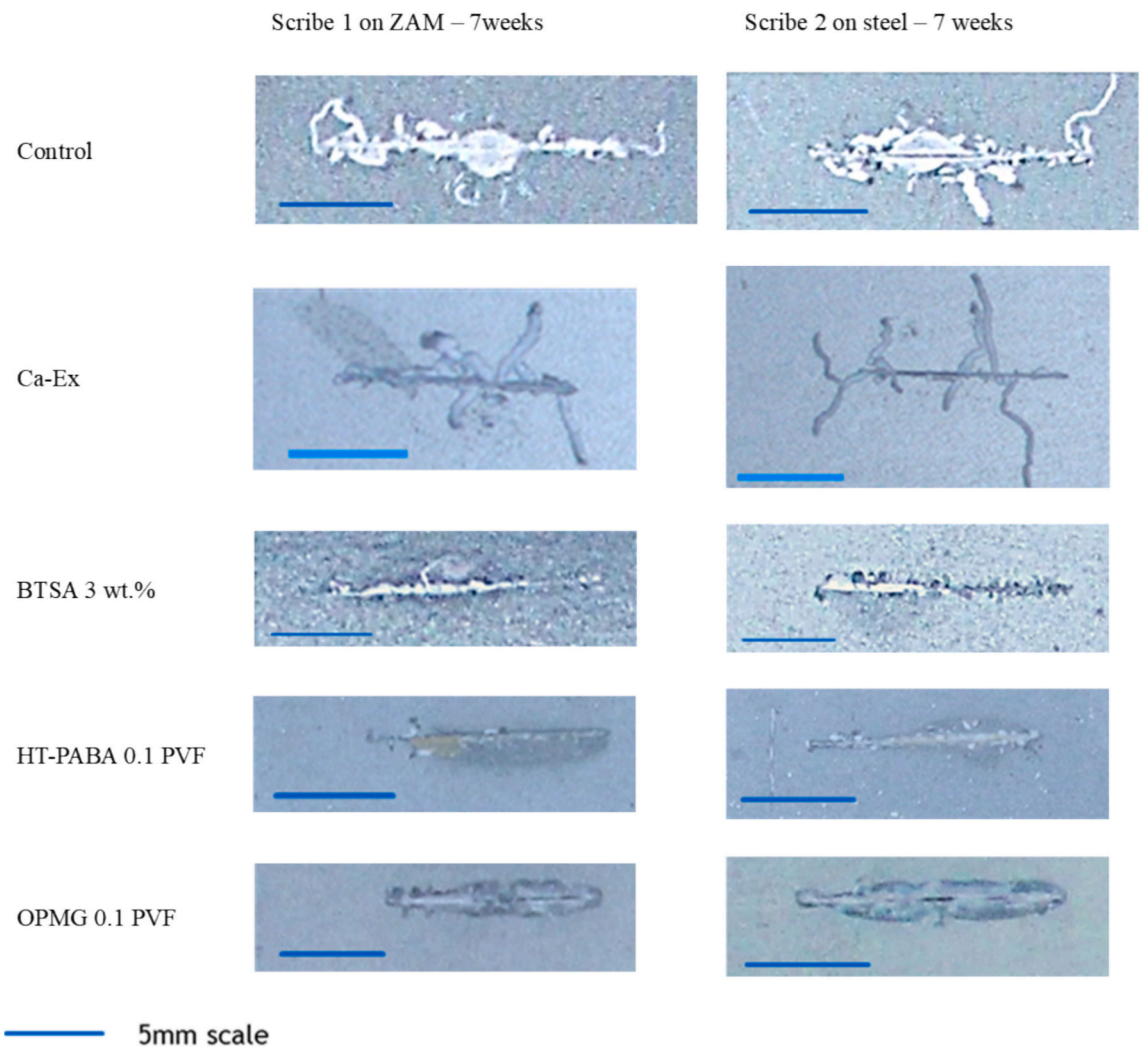

Fig. 8. Representative timelapse images of FFC produced on penetrative scribes 7 weeks from initiation with 2 μL of 1.5 M HAc for the control and inhibited PVB coated ZAM substrates at loadings of 0.1PVF and 3 wt% (BTSA). Scribe 1 corresponds to defects scribed down to the ZAM coating, Scribe 2-down to the steel.

decreased initial blister area that formed as well as a reduction in the number of discrete filaments that initiated compared to the control. However, limited inhibition to the propagation of the individual filaments was observed as seen by the lengths of filaments and the total observed corroded scribe areas.

The same three most effective inhibitors from the initial CD study (OPMG, HT-PABA, and BTSA) showed the greatest level of inhibition to the initial blister areas, overall corroded scribe areas as well as the length of filaments that extended past the defect site. With OPMG and HT-PABA clearly showing the greatest observed inhibition to both the number of filaments that initiated as well as a limited progression of the corroded scribe area observed even when the underlying steel was exposed (scribe 2).

BTSA was also effective at inhibiting the initial blister area that formed as well as the propagation of the corroded scribe area, but as can be seen in Fig. 8 a greater number of filaments initiated along the scribes compared to OPMG and HT-PABA, suggesting that the inhibitor was more effective during the propagation stage of FFC as more BTSA was released into the interfacial electrolyte once the filaments had undermined the PVB coating.

To further characterise the FFC kinetics the total corroded scribe areas (mm^2) were plotted against time for the control and inhibited coatings for scribe 2 in Fig. 9, with a zoomed in graphical inset provided to better deduce the rate progression for the most effective inhibitors (BTSA, HT-PABA, and OPMG). Where the kinetics for FFC on unpigmented PVB coated ZAM have been characterised previously, with the progression of FFC shown to increase linearly with time, indicative of the conservation of the electrolyte within the filament heads [32,59]. Moreover, this linearity implies that the distance between the principal cathodic (rear) and anodic (front) sites present within the filament heads remain constant throughout the FFC mechanism, as new cathodic sites develop underneath the PVB coating through the preferential dissolution of the $MgZn_2$ phases at the filament heads [32,59]. Whereas the rate kinetics for effective inhibited coatings during FFC on ZAM can be split into two distinct phases: an initial higher blister/filament initiation rate, followed by the reduced phase 2 kinetics. Where both the linear and reduced rate progressions can be seen clearly in Fig. 9 as both the control and Ca-Ex coatings increased linearly, whereas the other three inhibitors show a shift from linearity at longer holding times (~2–4 weeks). To evaluate the inhibitor efficiencies against the progression of the total corroded scribe areas the rate constants were determined through linear regressions of the plots in Fig. 9 with the relative inhibitor efficiencies calculated against the control coatings and summarised in Table 3.

Inhibitor efficiencies for the three most promising inhibitors showed similar overall efficiencies of ≥88 % with OPMG and BTSA showing a greater initial inhibition to the corroded area at week 2 compared to HT-PABA. While past 2 weeks the corroded area rate for all three inhibitors reduced significantly with OPMG and HT-PABA displaying the greatest

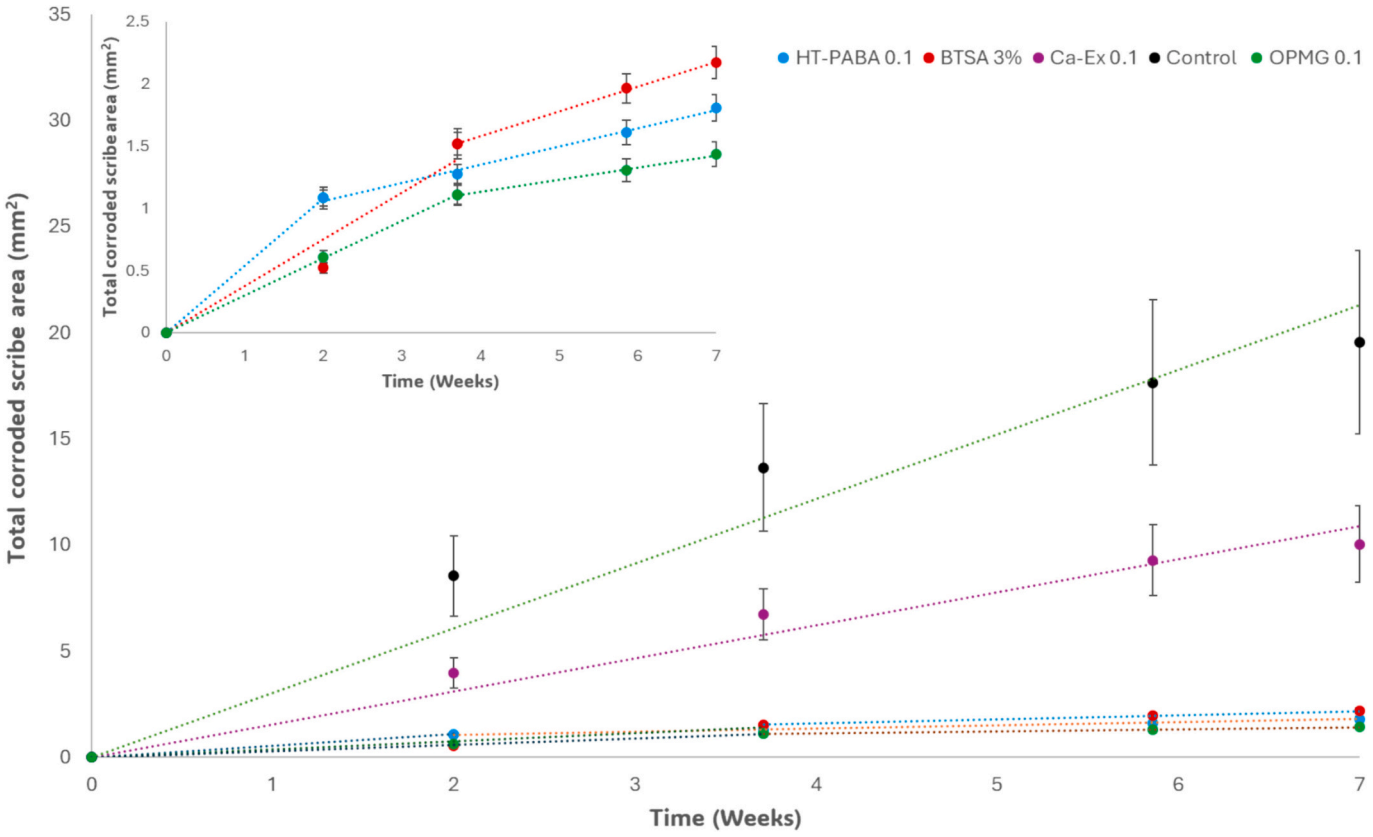

Fig. 9. Plot of the measured Total corroded scribe area as a function of time for the control and inhibited PVB films at inhibitor loadings of 0.1 PVF or 3 wt% (BTSA) for Scribe 2 (Steel). With a zoomed inset of the plot provided for the three most inhibitive coatings, with the error corresponding to ± one standard deviation from the average measured total corroded area from three repeat experiments.

Table 3
Summary of the overall FFC total scribe area rates for scribe 2 (steel) at inhibitors loadings of 0.1PVF or 3 wt%, as well as the determined inhibitor efficiencies based on the linear regression of whole plots in Fig. 9.

	dA/dt (mm^2 $week^1$) Scribe 2	Inhibitor efficiency (%)
Control	2.72	0.0
Ca-Ex	1.40	47.4
BTSA	0.33	88.1
HT-PABA	0.23	91.4
OPMG	0.20	92.6

inhibition to the propagation of the corroded scribe area while the filaments that initiated on the BTSA coatings continued to propagate past the scribe. With the results highlighting that all three inhibitor systems inhibited both the initiation of FFC as well as the propagation of the filaments.

To further investigate the inhibition efficiencies as a function of pigment loading a secondary systematic study was conducted where the three most promising inhibitors were loaded at different PVF'S, or wt %'s, with scribes only formed down to the ZAM layer (Scribe 2) used in this secondary screening. With the resultant total corroded scribe area rates and inhibitor efficiencies for phase 1 and 2 summarised in Table 4. Where K_1 and K_2 represent the rate constants for phases 1 and 2, with the error for the rate constants corresponding to one standard deviation from the mean of the 3 repeat experiments per inhibitor loading.

Table 4 shows that the increased pigment loadings resulted in an increased inhibition efficiency for all inhibitors with respect to both the initiation and phase 2 kinetics. With the increased loading of HT-PABA resulting in the greatest inhibitor efficiency increase for phase 1 (~15 %) with BTSA and OPMG only showing an increase of ~10 %, while

Table 4
Summary of the FFC total measured corroded Scribe 2 (Steel) area rate constants for the initiation phase (K_1), and secondary phase (K_2) for HT-PABA, OPMG and BTSA at inhibitors loadings of 0.05–0.1 PVF or 1–3 wt%. The determined inhibitor efficiencies for both phases versus the control are also shown with rate constant errors corresponding to ± one standard deviation of the measured K rate constants from 3 repeat experiments for each inhibitor loading.

Coating (loading)	K_1 (mm^2 $week^{-1}$)	t_i (weeks)	Inhibitor efficiency (%)	K_2 (mm^2 $week^{-1}$)	Inhibitor efficiency (%)
OPMG0.05	0.67 ± 0.03	4.00	81.7	0.19 ± 0.05	89.8
OPMG 0.1	0.30 ± 0.01	4.00	91.9	0.10 ± 0.02	94.6
HT-PABA 0.05	1.05 ± 0.05	4.00	71.7	0.33 ± 0.08	82.0
HT-PABA 0.1	0.51 ± 0.02	2.00	86.3	0.15 ± 0.03	91.9
BTSA 1 %	0.75 ± 0.04	4.00	79.8	0.58 ± 0.07	67.8
BTSA 3 %	0.41 ± 0.02	4.00	89.0	0.20 ± 0.04	89.0

BTSA displayed the greatest increase in inhibition efficiency (~20 %) for phase 2. HT-PABA followed by OPMG also showed an increased inhibition efficiency to the phase 2 kinetics through the increased loadings, with HT-PABA showing a greater change as was expected based on the results in Fig. 8 and Table 4 that showed that HT-PABA primarily impacted the propagation kinetics for FFC. Where the results from the study show that the three most promising inhibitors from the CD study also have a profound effect against FFC with the order reversed during FFC with the inhibition mechanisms for the inhibitors against CD and FFC further discussed in Section 3.4.

3.3. In solution inhibition

3.3.1. Linear polarisation testing

To investigate the inhibitor pigments screened in the previous sections, bare ZAM substrates were immersed in 3.5 wt% NaCl $_{(aq)}$ solutions and potential-dynamically tested according to the methodologies in Sections 2.4 and 2.6. Where either the inhibitor (BTSA, and OPMG) or the soluble inhibitor species (Ca^{2+}, and PABA) were directly added to the NaCl solutions and then adjusted to pH 7. Where the pH of the inhibited solutions was adjusted to allow for a direct comparison to the initiating electrolyte environment present within the CD experiment (local defect site) as during the initiating stage for CD the release of inhibitor species would only occur once the delamination front had progressed past the defect site (minimal change in local pH). Moreover, the pH was also adjusted to allow for a direct comparison between the inhibitor species as OPMG's solubility within the solution was highly dependent on the pH of the solution and thus the supernatant of the saturated solution was used in the following testing to provide a consistent concentration. The specimens were polarised once every hour with R_p values (ohms. cm^2 $\times 10^{-3}$) obtained up to 12 h for each electrolyte with a total of three repeats averaged and plotted as function of time in Fig. 10. Moreover, the evolution of the open circuit potential (OCP) for the three most effective inhibitors during the experiment are shown in Fig. 11, with the error bars seen in both plots corresponding to one standard deviation from the averaged R_p and OCP values.

Figs. 10 and 11 show that through the direct inhibitor additions within the solutions, an increase in the measured R_p values compared to the control 3.5 wt% solution were observed as well as a consistent stable OCP establishing over the course of the experiment for all solutions indicative of anodic deactivation. With the greatest increase (several magnitudes) in the measured R_p values seen for BTSA and the 4 g/L (Saturated) OPMG solutions. PABA showed the next highest increase in measured R_p compared to the control and the $CaCl_2$ inhibited solutions but showed a reduced expected inhibition level compared to the observed inhibitor efficiencies during CD and FFC. With this observation suggesting that the inhibition performance seen for HT-PABA during CD (chloride electrolyte) was either promoted by the alkalinity within the underfilm electrolyte or the ion exchange mechanism from the hydrotalcite pigment. Where the ion exchange mechanism from HT was highly effective against FFC during a previous study but has been shown to be not as effective on its own during CD [20,32].

3.3.2. Polarisation testing for PABA, BTSA and OPMG

Following the results in Section 3.3.1 potentiodynamic sweeps for the anodic and cathodic branches for OPMG PABA and BTSA inhibited solutions were conducted following the methodology in Section 2.6. The anodic and cathodic branches were measured independently on fresh samples and using fresh electrolytes for a total of three repeats generated per iteration. The corresponding averaged responses were then merged and plotted in Fig. 12 with all three inhibited solutions resulting in a positive shift in the measured OCP vs. the control. Shifts in the measured OCP's of +30 mV, +125 mV and +134 mV for PABA, OPMG, and BTSA respectively were observed with the calculated values of i_{corr} taken as 1.85×10^{-6} A for the control and 4.13×10^{-7} A, 1.469×10^{-7} A, and 1.502×10^{-7} A for the other inhibitors respectively. Moreover, from the limited change in the shapes of the cathodic branches, paired with the shift in the OCP, in can be concluded that all three inhibitors act primarily as net anodic inhibitors at pH values of 7 and at the specific chloride concentration used in these tests. BTSA has previously been shown to exhibit mixed inhibitory properties where the specific mechanism of inhibition has been shown to be dependent on the concentration of the inhibitor within the solution, where at high concentrations it acts predominately as a net anodic inhibitor [72].

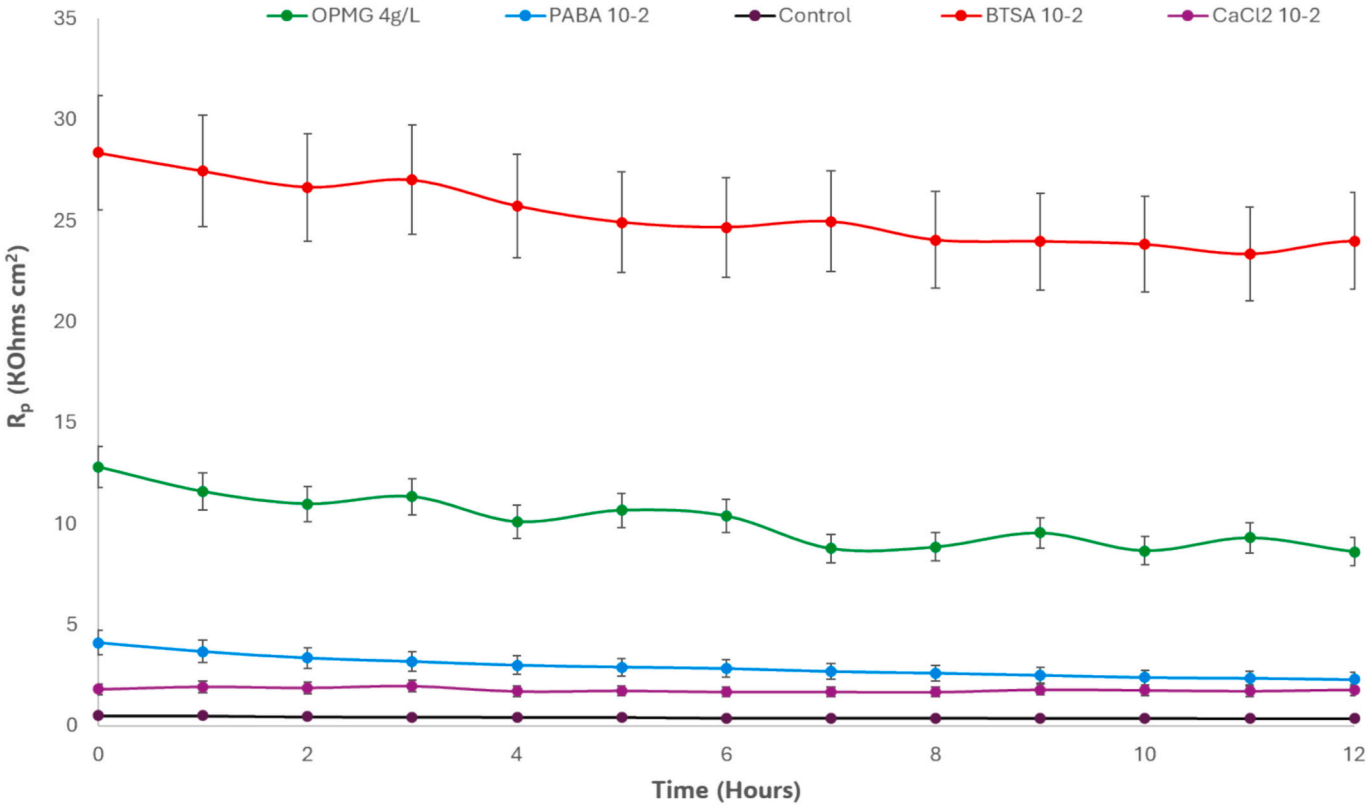

Fig. 10. Plots of calculated R_p values as a function of time for ZAM samples immersed in 3.5 wt% NaCl $_{(aq)}$ pH 7 control and inhibited solutions containing either 10^{-2} M direct pigment additions (BTSA, PABA, $CaCl_2$) or the supernatant of a saturated inhibited solution (OPMG) up to 12 h from immersion. With the error corresponding to ± one standard deviation from the average calculated R_p values from 3 repeat experiments. The polarisation scan rate was 0.166 V s^{-1}.

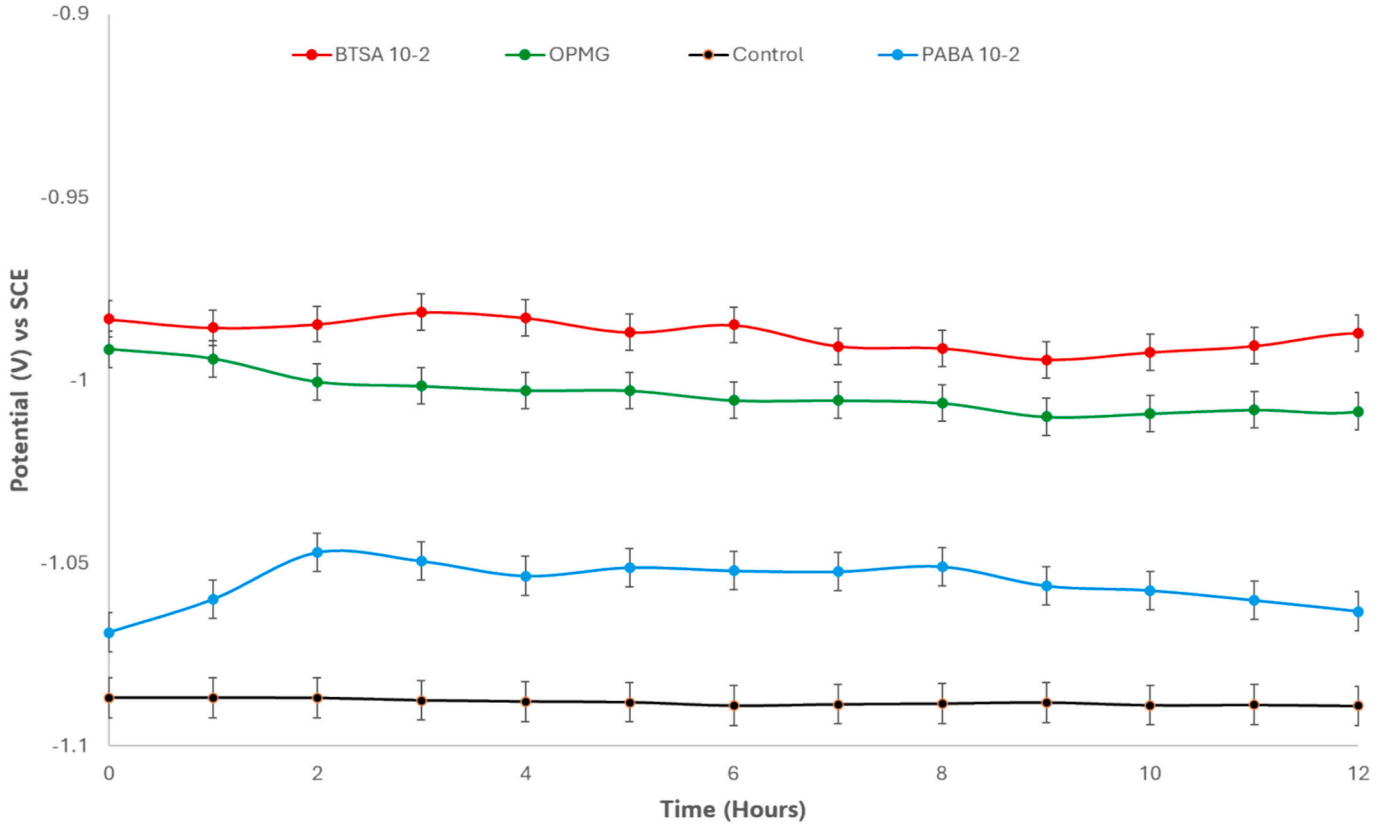

Fig. 11. Progress of the open circuit potential for the immersed ZAM substrates within the control and inhibited 3.5 wt% pH 7 NaCl $_{(aq)}$ solutions containing either 10^{-2} M (BTSA, PABA, $CaCl_2$) or the supernatant of a saturated inhibited solution (OPMG) up to 12 h from immersion. With the error corresponding to ± one standard deviation from the average calculated OCP values from 3 repeat experiments. The polarisation scan rate was 0.166 V s^{-}.

3.3.3. *Cut-edge SVET testing*

The SVET was utilised to investigate the localised cut-edge corrosion that occurred on the ZAM coated Steels immersed in inhibited 3.5 wt% NaCl $_{(aq)}$ solutions prepared according to Sections 2.4 and 2.7. Where the data generated from the SVET was utilised to generate normalised current density maps (Fig. 13), that represent the time resolved localised anodic and cathodic activities over the immersed cut edge surfaces at hours 1, 6, 12, 18, and 24. With the blue and red regions within the current density maps in Fig. 13 representing the resolved cathodic and anodic activities respectively, and the white regions (zero current density) representing either the non-conductive resin or the passivated/non active regions. As expected, the plots in Fig. 13 show that the ZAM coatings (either side of the steel) sacrificially protected the exposed steel, as the anodic activity is restricted over the exposed zinc layers throughout all the resolved current density maps. Where the anodic activity for the control, BTSA, and PABA electrolytes can be seen to preferentially occur on one of the ZAM layers, due to the local electrochemical asymmetry between the two zinc layers. With this observation shown to occur previously for SVET resolved NaCl immersed zinc cut edges, where variations in the surface oxides, phase distributions, local electrolyte and surface finish between the two zinc layers lead to the formation of preferential anodic sites [73,74].

The anodic attack during the corrosion of immersed ZAM cut edges typically occurs on the exposed zinc layers with the anodic dissolution leading to the indiscriminate dissolution of the various metal intermetallics present to release Zn^{2+}, Mg^{2+}, and Al^{3+} cations due to the restricted cathodic ORR over the steel. This development of electrochemical activity across the cut edge results in the distribution of the local pH, where an alkaline region develops over the steel and a low pH near the anodically active ZAM (metal hydrolysis of Zn^{2+}, and Al^{3+} ions) leading to the precipitation of metal hydroxides over the steel [59,70,73–75]. Where previous literature has shown the development of two distinctive zones that form over the steel: a region covered with the corrosion precipitation (zone 1) and the bare uncovered steel (zone 2) with the location of precipitation controlled by the solubility limits of the metal hydroxides within the varying local pH zones [70,74].

Fig. 13 shows that the control sample displayed a consistent high anodic activity for the first three scans, while after 12 h more localised and intense anodic features developed across the (left) exposed ZAM layer as a well as a passivated region between the anodic and cathodic sites. PABA showed a slight reduction in the intensities of the anodic activity over the course of the experiment (compared to the control) with a larger corrosion product layer formed within the central steel as seen by the reduced cathodic area (higher zero intensity) in Fig. 13. Whereas BTSA showed a reduced initial anodic area (compared to the control) during the first scan as well as a reduction in the measured anodic and cathodic intensities that formed on the ZAM and steel surfaces respectively. OPMG showed a significant decrease in the observed total anodic area for the first scan compared to the control, but with more localised discrete anodic sites developing along both sides of the exposed ZAM layers, where OPMG was the only inhibitor to display this behaviour throughout the whole experiment. Both OPMG and BTSA over the course of the experiment resulted in reductions in the measured anodic and cathodic activities across the specimens, with a more transient shift to passivation seen for OPMG when compared to BTSA. However, OPMG by the 24 h scan showed a more passivated surface compared to the control, BTSA, and PABA which was attributed to the formation of adherent precipitation films that acted to passivate the exposed cut edge as seen by the increased white inactive sites that developed across the steel surface. Which in turn would limit the available sites for the cathodic ORR to occur and in turn limit the driving force for the metal dissolution reaction.

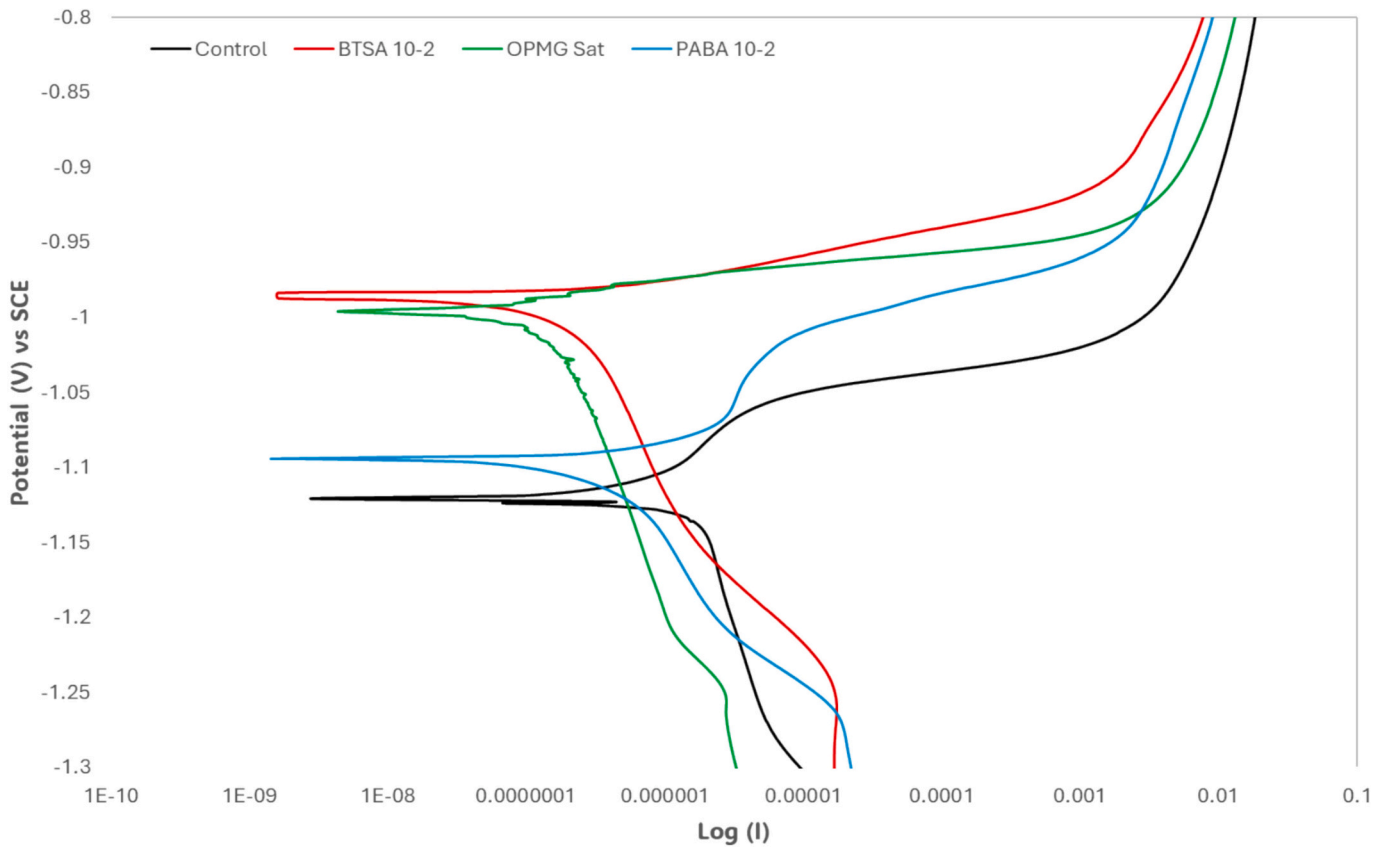

Fig. 12. Potentiodynamic polarisation curves for the merged anodic and cathodic branches for ZAM surface samples immersed in 3.5 wt% $NaCl_{(aq)}$ pH 7 control (Black) and inhibited solutions containing either 10^{-2} M BTSA (Red), 10^{-2} M PABA(blue) and the supernatant of the saturated OPMG solution (Green). With the potentiodynamic scan rate set at 0.166 V s^{-1}. (For interpretation of the references to color in this figure legend, the reader is referred to the web version of this article.)

To deduce the inhibitor efficiencies during the SVET experiments a plot of the total measured anodic current densities per scan (Fig. 14) as well as the calculated total metal (zinc) losses (Table 5) were generated for all tested inhibitors according to Section 2.7. With the results showing that the inhibitor additions of PABA, BTSA and OPMG all resulted in the inhibition to the anodic metal dissolution reactions as seen by the reduction in the observed anodic activities in Figs. 13 and 14 despite the high cathodic to anodic area disparity as well as cathodic inhibition to the central exposed steel. With Fig. 14 visually representing the observed change in the total measured anodic activity seen on the current density maps in Fig. 13, where the total anodic current density for OPMG initially increased for the first 6 h (formation of local intense anodic features in Fig. 13), followed by a progressive reduction in the measured total anodic current density over the remainder of the experiment. With the observed total scan anodic current density dropping below the anodic current density for BTSA after ~19 h. BTSA showed a more continuous drop in the measured anodic current density, where initially a more rapid drop can be seen between hours 1–6 and then a more gradual drop occurs due to the possible saturation of the precipitated mixed metal organic film over the exposed steel or the limited availability of metal cations within the solution. PABA displayed a limited change in the measured total anodic activity across the experiment with a constant value establishing in Fig. 14. However, all three inhibitors displayed total anodic activities below the control during every scan as well as an increased passivation of the cathodic area over the steel.

Table 5 summarises the resultant overall inhibitor efficiencies for PABA (38 %), OPMG (66.8 %) and BTSA (68 %) against the anodic dissolution of the ZAM coatings. Where it should be noted that the SVET testing and metal loss calculations employed here have several limitations (as discussed in Section 2.7) with the technique used exclusively here to compare the screened inhibitors as well as spatially resolve the change in anodic and cathodic features that developed over the course of the experiment, opposed to the accurate determination of the zinc metal coating loss [59–62,75].

3.4. Inhibition mechanisms for BTSA, HT-PABA and OPMG

The electrochemical testing paired with the inhibitor ranking orders derived from the CD and FFC studies showcase that the three most promising inhibitors outperform the commercial standard Ca-Ex pigment and inhibit in the presence of both alkaline (pH 10–12) chloride electrolytes and acidic mediums (pH 2–5). With their proposed inhibition mechanism furthered discussed below for both the inhibition to CD and FFC.

3.4.1. HT-PABA inhibition

HT-PABA additions to the model PVB coatings resulted in the inhibition to both t_i (initiation phase) as well as the rates of coating delamination during CD, with the mechanism controlled by the cation insertion at the interfacial delamination front to pull down the potential for the ORR to proceed [63,64] PABA was released from the HT pigment through the anion exchange mechanism between Cl^- and OH^- anions within the defect and underfilm electrolyte regions respectively as they made contact with the PVB coating [20].

The main inhibitory mechanisms proposed for HT-PABA during CD is the formation of PABA-Zn complex films that chelate or adsorb onto the positively charged corroding metal surfaces (Zn^{2+}) at the coating/defect boundary or underneath the delaminated coating [38,46]. Which would contribute to the observed delay in the initiation of CD as well the

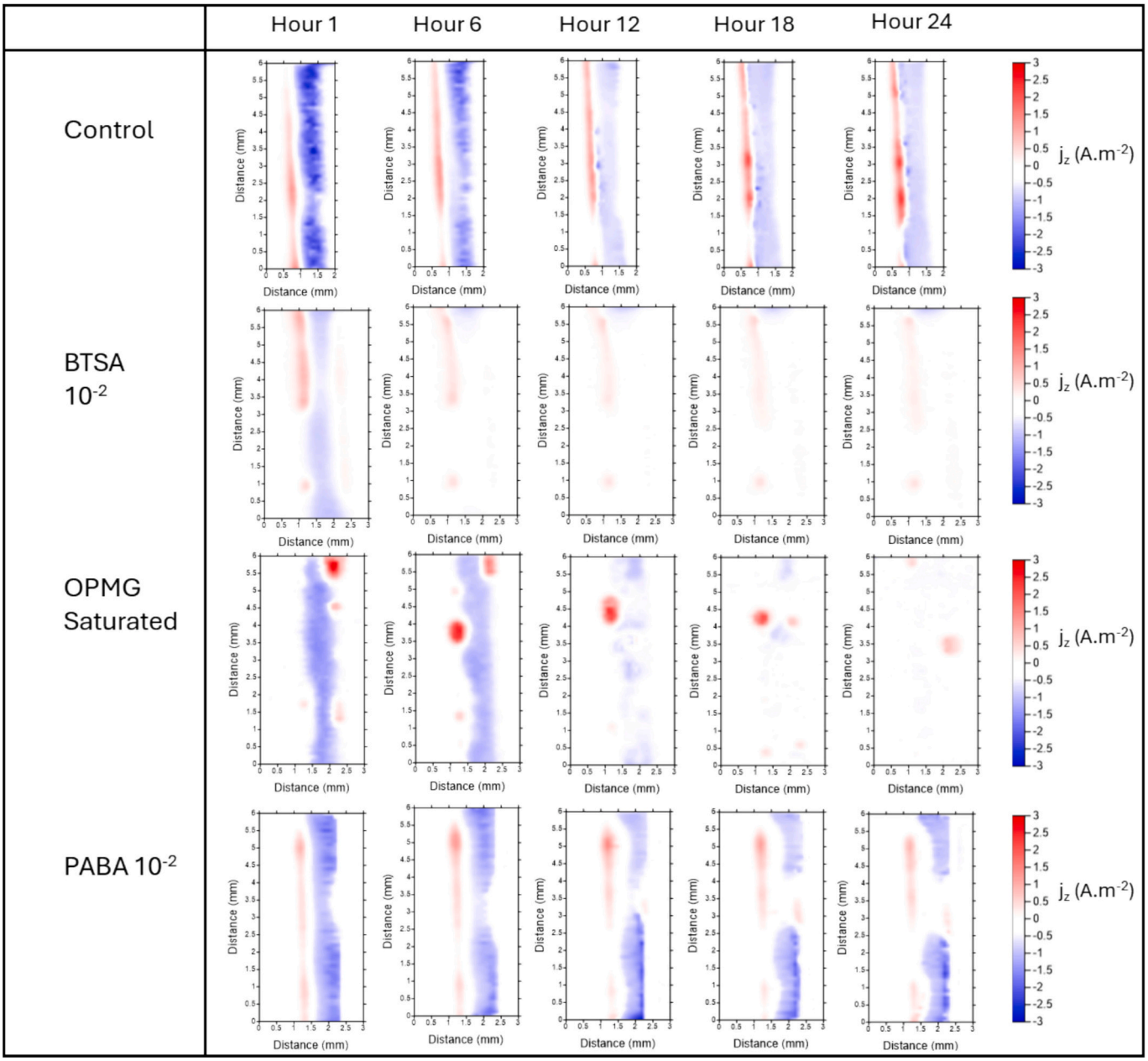

Fig. 13. Summary of the 2D current density SVET maps for ZAM cut edge samples immersed in 3.5 wt% NaCl $_{(aq)}$ pH 7 control and inhibited solutions containing either 10^{-2} M BTSA, 10^{-2} M PABA or the supernatant of the saturated OPMG solution after 1, 6, 12, 18, and 24 h with the scale bar for all the experiments in A/m^2.

inhibition to the rate kinetics of coating delamination. Moreover, the formation of the PABA-Zn complexes is expected to be promoted in more alkaline higher pH's (delamination front) due to the increased anodic activity at the zinc surface (Eqs. (9) and (10)) and the deprotonation of the COO^- groups. As the chemical structure of PABA consists of an aromatic benzene ring substituted with amino (NH_2) and carboxylic acid (COOH) groups, where at pH values above >5 PABA would predominately exist in its anionic state with the carboxylic groups predominately deprotonated and the amino group in a neutral state [40,42]. Moreover, the release of PABA from the PVB coating would result in the decrease in the local underfilm pH that in turn would promote the formation of insoluble zinc hydroxide as seen by the equilibrium reactions (Eqs. (9) and (10)) once the solubility limit for zinc hydroxide (K_{sp} 1.2 × 10^{-17}mol^{3}dm^{-9}) is reached [19]. Where both the production of the Zn-PABA complexes and promotion of zinc hydroxide formation underneath the underfilm region as well as at the coating/defect boundary would result in the formation of a tortuous path that would inhibit both the migration of Na^+ cations to the delamination front as well as disrupt the ohmic drop between the anodic defect and delamination front (driving force for cation insertion) [63,64]. However, it should be noted that in the presence of Cl^- ions a competing reaction could occur between PABA and Cl^- ions to complex with Zn^{2+} as seen in Eq. (12), that in turn would lead to the formation of soluble zinc chlorides. However, as Cl^- ions remain local to the defect site as well as the anion exchange mechanism for HT, the Cl^- concentration within the underfilm region would be further limited and thus increase the likelihood of the Zinc-PABA passive films to form [3,19].

$$Zn^{2+} + 4Cl^- \rightarrow (ZnCl_4)^{2-}\ (Soluble\ complex) \quad (12)$$

In addition, the amino groups located on the benzene ring could also act to preferentially react with free radicals generated through the ORR at the delamination front and limit the degradation of the coating/metal

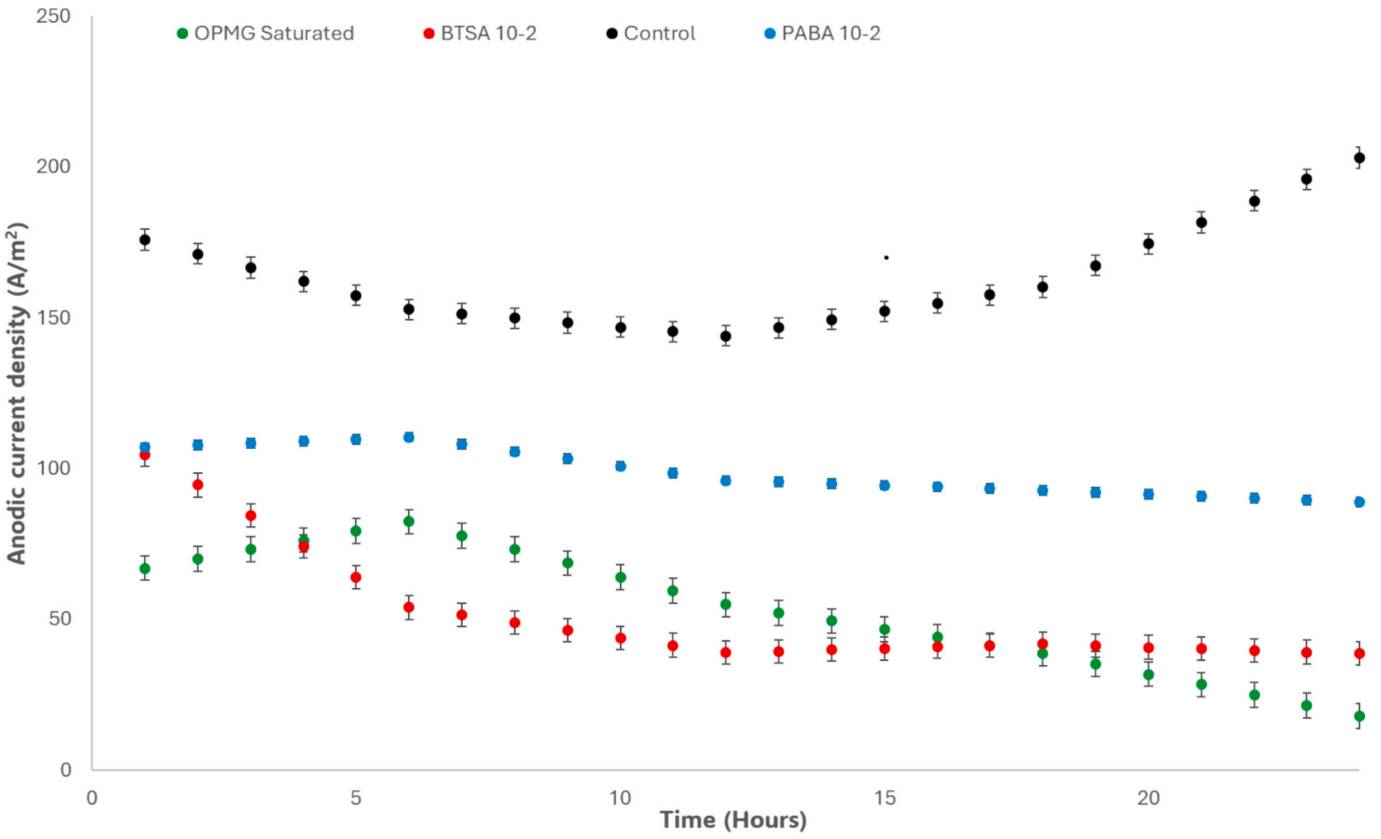

Fig. 14. Plots of total Anodic scan current density as a function of time for each scan via SVET for the ZAM cut edge samples immersed in 3.5 wt% $NaCl_{(aq)}$ pH 7 control (black) and inhibited solutions containing either 10^{-2} M BTSA (Red), 10^{-2} M PABA (blue) or the supernatant of the saturated OPMG solution (green). (For interpretation of the references to color in this figure legend, the reader is referred to the web version of this article.)

Table 5
Total cut-edge metal (Zinc) losses and inhibitor efficiencies for the control, BTSA 10^{-2} M and saturated OPMG 3.5 wt% pH 7 $NaCl_{(aq)}$ solutions after 24 h via SVET. With errors corresponding to ± one standard deviation from the average derived metal mass loses from 3 repeat experiments.

Inhibitor	Total calculated mass loss after 24 h's (mg)	Inhibitor efficiency
Control ZAM	0.221 ± 0.02	N/A
BTSA 10^{-2}	0.071 ± 0.01	68.0 %
OPMG Saturated	0.074 ± 0.01	66.8 %
PABA 10^{-2}	0.138 ± 0.03	38.3 %

interfacial bonds as seen in Eq. (13) [20,67]. Where R· represents the free radical species generated at the delamination front (HO^{2-}, O^{2-}, OH), Ar-NH_2 is the aromatic PABA structure and Ar-NH• is the generated nitrogen centred aromatic radicals. Where the aromatic ring present could act to stabilise PABA formed radicals through distributing unpaired electrons and ultimately reducing the resultant rate of coating detachment (increased delay in CD kinetics) [48,51].

$$R^{\cdot} + Ar - NH_2 \rightarrow RH + Ar - NH^{\cdot} \quad (13)$$

HT-PABA during FFC showed inhibition to both the total corroded scribe area generated as well as shift from linear controlled kinetics that was concurrent with previous HT inhibitory studies for FFC on ZAM coated substrates [32]. Where the release of PABA as well as naturally occurring carbonate species was facilitated by the anion exchange mechanism in the presence of the acetate anions present within the defect site and electrolyte filled filament heads [32]. Where PABA could adsorb onto either the anodic sites present at the defect/coating interfacial boundaries, the filament heads or preferentially at the alkaline cathodic sites (rear of the filament head). Where the resultant PABA metal complex films could result in the passivation of $MgZn_2$ phases as well as the corrosion product zinc surfaces present within the tail, that in turn would inhibit the transport of O_2 to the differential aeration cell (filament head) and reduce the driving force for filament propagation [31,32]. Where Eqs. (14)–(16) show the proposed formations of the Zn, Mg, and Al complexes that could form through reacting with the metal cationic species released during metal dissolution. This suggested mechanism likely to occur due to the thermodynamic tendency of the Zn^{2+}, Mg^{2+} and Al^{3+} cations to form more stable low solubility complexes with the deprotonated carboxylate groups compared to a previous work by Bazzi et al. who demonstrated that PABA predominately interacted with copper surfaces through physisorption due to weak dispersive forces and the low Gibbs free energy of formation for Cu_2O ($-146 kJmol^{-1}$) [76,77].

$$Zn^{2+} + 2PABA^{-} \rightarrow Zn(PABA)_2 \quad (14)$$

$$Mg^{2+} + 2PABA^{-} \rightarrow Mg(PABA)_2 \quad (15)$$

$$Al^{3+} + 3PABA^{-} \rightarrow Al(PABA)_3 \quad (16)$$

Moreover, both PABA and carbonate ions present within the HT pigment could act to neutralise the low pH's present at the scribe and filament front electrolytes either through a protonation-deprotonation equilibrium mechanism or an acid-base interaction respectively. Where both mechanisms are facilitated by an anion exchange mechanism between the acetate (Ac) ions and either PABA or Carbonate species as seen in Eqs. (17)–(19) [32]. In the case of the acid-base reaction in Eq. (20) the formation of water results in an increase in the filament head electrolyte volume, which in turn results in the increase in local pH within the filament head [32].

$$2HAc_{(aq)} + CO_{3\ HT}^{2-} \rightarrow 2Ac_{HT}^{-} + CO_{3\ (aq)}^{2-} + 2H^{+} \quad (17)$$

$$HAc_{(aq)} + PABA_{HT}^{-} \rightarrow Ac_{HT}^{-} + PABA_{(aq)}^{-} + H^{+} \quad (18)$$

$$PABA^{-} + H^{+} \leftrightarrow PABA - H \quad (19)$$

$$2HAc_{(aq)} + CO_{3\ (aq)}^{2-} \rightarrow H_2O_{(l)} + CO_{2\ (g)} + 2Ac_{(aq)}^{-} \quad (20)$$

The inhibition mechanism has been shown to occur previously for commercial HT formulated PVB coated ZAM substrates undergoing FFC initiated with HAc [32]. With the observed inhibition to both the initial corroded area and propagation of the FFC scribe areas seen for HT-PABA coatings within this study concurrent with the proposed mechanism.

3.4.2. OPMG inhibition

For OPMG loaded PVB coatings during CD both an increase in t_i and a reduction in the delamination rate was observed, with the inhibition to the delamination rate attributed to the deposition of either Zinc or Magnesium phosphate precipitate film as seen in Eqs. (21)–(22).

$$2HPO_4^{2-} + 2OH^{-} + 3Zn^{2+} \leftrightarrow Zn_3(PO_4)_2 + 2H_2O \quad (21)$$

$$2HPO_4^{2-} + 2OH^{-} + 3Mg^{2+} \leftrightarrow Mg_3(PO_4)_2 + 2H_2O \quad (22)$$

Where the form in which phosphate is present within the electrolyte is governed by the pH as seen by the dissociation of phosphoric acid in Eqs. (23)–(25) [19].

$$H_3PO_4 \leftrightarrow H_2PO_4^{-} + H^{+}\ [pK_{a1} = 2.14] \quad (23)$$

$$H_2PO_4^{-} \leftrightarrow HPO_4^{2-} + H^{+}\ [pK_{a2} = 7.2] \quad (24)$$

$$HPO_4^{2-} \leftrightarrow PO_4^{3-} + H^{+}\ [pK_{a2} = 12.4] \quad (25)$$

As an alkaline environment is generated at the cathodic delamination front (pH's > 10) it can be estimated that the phosphate species released from the PVB coating into the underfilm electrolyte would take the form of hydrogen phosphate HPO_4^{2-} following the reaction in Eq. (25). Therefore, as the solubility constant for zinc phosphate (K_{sp} 9 × $10^{-33}mol^3dm^{-9}$) and magnesium phosphate (K_{sp} 1 × $10^{-25}mol^3dm^{-9}$) are several orders of magnitude lower than zinc hydroxide and magnesium hydroxide (K_{sp} 1.8 × 10^{-11} mol^3dm^{-9}) it is likely that the phosphate precipitate films would preferentially form due to the presence of Zn^{2+} (Eqs. (9) and (10)) and Mg^{2+} (OPMG) cations within the underfilm electrolyte [19,74,75,78]. Moreover, as OPMG contains an amine group with a pKa value of ~(9–10) it can therefore be reasoned that within the electrolyte well, the protonated amine groups could electrostatically adsorb onto the negatively charged ZnO layers present further limiting the dissolution of the amphoteric oxide layers. With the adsorption and precipitate films that form resulting in the formation of a tortuous pathway for cation insertion at the interfacial delamination front region as well the stabilisation of the zinc oxide layers present underneath the PVB coatings [64,65]. Which in turn would reduce the driving force for CD (ohmic drop between the defect and delamination front) explaining the predominant inhibition to the rate progression of CD opposed to the initiation phase seen in Section 3.1 as the delay in t_i was constant across the different loadings of OPMG.

The presence of OPMG during FFC corrosion resulted in the greatest observed inhibition to both the initial corroded scribe area as well the propagation of filaments, with a shift from linearity observed after ~4 weeks. Due to the low pH's present within the defect site (acetic acid) as well as at the front of filament heads it can presumed that the amino (NH_2) groups present to be primarily in their protonated form, with the form of the phosphate anions governed by the local pH according to Eqs. (23)–(25). Where the presence of the phosphate anions within the electrolyte would act to buffer the local acidic pH through absorption of H^+ ions as well as forming metal phosphate complexes according to Eqs. (23) and (26)–(27) at the anodes (head), defect/coating boundary or at the cathodic rear portion of the filament heads (Eqs. (21)–(22)). That in turn would inhibit the preferential dissolution of $MgZn_2$ phases and stabilise the precipitated corrosion products formed at the defect sites/tail regions. With the protonated amino groups present aiding in the adhesion and stability of the films formed through hydrogen bonding and the lone pairs from the N and O groups [43,44,72]. Where the proposed inhibition mechanisms explain the limited number of filaments that initiated from the scribes as well as the concentration of corrosion product that formed local to the scribe defects. Furthermore, as seen in Table 4 the inhibition to the initial rates for the total corroded scribe areas was strongly influenced by the inhibitor loadings suggesting that a critical presence of the phosphate species was required to inhibit the progression of the anodic undermining as well as neutralise the acidic pH. Where the assumption that a critical concentration of OPMG was required is further strengthened through the fact that no delay in FFC kinetics was observed only the inhibition to the formation and propagation of discrete filaments.

$$3Zn_{(aq)}^{2+} + 2H_2PO_{4\ (aq)}^{-} \rightarrow Zn_3(PO_4)_{2\ (s)} + 4H^{+} \quad (26)$$

$$3Mg_{(aq)}^{2+} + 2H_2PO_{4\ (aq)}^{-} \rightarrow Mg_3(PO_4)_{2\ (s)} + 4H^{+} \quad (27)$$

3.4.3. BTSA inhibition

BTSA during CD showed the greatest level of inhibition to t_i as well as to the rates of coating delamination compared to the other inhibitors. BTSA comprises of a benzothiazole ring containing heteroatoms (N,S) where at pH's >10 the thiolate S^- and the carboxylate group COO^- would be expected to be primarily in their deprotonated forms [53,54,72,79]. Therefore, it can be reasoned that BTSA would chelate with Zinc ions present at the defect/coating boundary and underneath the underfilm electrolyte to form a chemisorbed passive film according to Eq. (28). Moreover, the presence of BTSA could also act to reinforce and stabilise the zinc oxide surfaces present through the formation of a Zn-BTSA-ZnO hybrid film according to Eq. (29).

$$BTSA^{2-} + Zn_{surface}^{2+} \rightarrow Zn - BTSA_{adsorbed} \quad (28)$$

$$(Zn - BTSA) + ZnO \rightarrow Zn - BTSA - ZnO\ (hybrid\ protective\ film) \quad (29)$$

Where this proposed mechanism would explain the increased time for CD kinetics to establish as well as the reduction in delamination rates observed for the BTSA inhibited PVB coatings, as the formation of the BTSA films and stabilisation of the ZnO layers would provide a tortuous pathway for cation insertion at the delamination front as well as limiting the anodic dissolution of the metal oxide layers at the coating/defect boundary and underneath the organic coatings [3,20]. In addition, through the release of BTSA from the PVB coating the local underfilm electrolyte pH would reduce (generation of H^+) thus promoting the formation of insoluble zinc hydroxide layers (Eqs. (9) and (10)) and thus could result in the disruption of the ohmic drop (driving force) between the anodic defect site and the cation free interfacial coating boundary [19,20,63,64,72]. Where the inhibition performance of BTSA to CD on HDG has been previously shown to be strongly influenced by the concentration of the inhibitor within the electrolyte, with higher concentrations adsorbing strongly to the organic-coated metal surfaces resulting in the stifling of the undefilm ORR and further dissolution of amphoteric zinc oxide, which would explain the limited change of inhibition efficiency past a critical concentration of BTSA within the PVB coatings [72].

For FFC, BTSA loaded PVB displayed a profound inhibition to both the initial blister/corroded area local to the scribe as well as the propagation of FFC. With a minimal corroded area observed compared to the control but with a larger number of filaments observed to initiate and propagate past the scribes compared to OPMG and HT-PABA loaded coatings. At the expected low pH at the scribe and filament heads, the benzothiazole ring, thiolate and carboxyl groups present would exist in

their protonated forms, thus suggesting a higher level of interaction at the cathodic (rear) sites [53,54,72]. The presence of both Mg^{2+} and Zn^{2+} cations within the filament electrolyte promotes the formation of compact mixed coordinate metal organic complexes that could precipitate to passivate the ZAM surface within the tail regions and exposed iron [79]. The increased inhibition seen in the propagation phase opposed the initiation phase for BTSA loaded PVB is attributed to the limited availability of BTSA and metal cations initially within the defect site as well as the initial acidic pH [72].

4. Conclusions

The corrosion behaviour of two zinc based alloy coated steels in the presence of a range of emerging environmentally friendly corrosion inhibitor technologies have been successfully evaluated against CD and FFC that occur on either HDG or ZAM substrates, respectively. Where all alternative inhibitor technologies screened led to a reduction in the observed initiation and progression rates for each mechanism. With the alternative inhibitor technologies shown to outperform the industry Ca-Ex pigment by ~20 and 40 % during CD and FFC, respectively. The observed inhibition efficiencies of CD take the following ranking order of: BTSA > HT-PABA > OPMG > Ca-Ex and for FFC OPMG > HT-PABA > BTSA > Ca-Ex, with the three alternative inhibitors showing inhibition efficiencies >78 % and >88 % at their highest inhibitor loadings against the control PVB coatings, respectively. Moreover, this work expands on the limited literature surrounding the inhibition of FFC on ZAM coated substrates using commercial grade functionalised alternative inhibitor systems that have also been shown to be effective against CD on HDG substrates. This work highlights possible alternative inhibitor systems that could be formulated into organic primers to provide cross-functional corrosion protection solutions that cover a range of zinc based alloy coated steels.

Furthermore, the inhibition performance for HT-PABA, OPMG and BTSA was investigated through potentiodynamic and polarisation testing of the immersed ZAM substates immersed in inhibited 3.5 wt% pH 7 $NaCl_{(aq)}$ solutions. Where OPMG and BTSA showed the greatest level of inhibition to the corrosion current through significant increases in the calculated R_p values (several orders of magnitude) as well as revealing that both inhibitors act as net anodic inhibitors through shifting the OCP by +125 mV and +134 mV, respectively.

Lastly the three most promising inhibitors were successfully evaluated at their ability to suppress the zinc metal loss for immersed ZAM cut-edge specimens immersed in inhibited solutions. With OPMG and BTSA inhibiting the SVET derived total metal (zinc) losses by ~67 % vs the control over a 24 h immersion period. With the mechanisms of inhibition for both attributed to the formation of metal inhibitor complex films that precipitated over the steel. Future work is required to evaluate the long term protection afforded by the alternative inhibitor technologies tested when loaded into fully formulated coil coatings, the possible synergistic effects afforded by mixed inhibitor loadings, and the influence of pH during the electrochemical characterisation of the inhibitors within chloride and chloride free solutions representative of the underfilm electrolyte during CD.

CRediT authorship contribution statement

Gwynfor Callaghan: Writing – review & editing, Writing – original draft, Visualization, Validation, Methodology, Investigation, Formal analysis, Data curation, Conceptualization. **Sonny Ngo:** Supervision. **Geraint Williams:** Writing – review & editing, Supervision.

Declaration of competing interest

The authors declare the following financial interests/personal relationships which may be considered as potential competing interests:

Sonny Ngo reports a relationship with Beckers Group that includes: employment. Geraint Williams reports a relationship with Swansea University that includes: employment and funding grants. Gwynfor Callaghan reports a relationship with Swansea University that includes: funding grants and non-financial support. If there are other authors, they declare that they have no known competing financial interests or personal relationships that could have appeared to influence the work reported in this paper.

Acknowledgements

This work was sponsored by: Beckers Industrial Coatings, the EPSRC as part of the centre for Doctoral training in Functional Industrial Coatings (COATED) grant reference (EP/S02252X/1). The author would like to thank Beckers Industrial Coatings, the EPSRC, Swansea University, Tata steel and COATED M2A for the funding, materials and support during the EngD studentship. In addition, special thanks to Prof Geraint Williams, Dr. Sonny Ngo, and Dr. Natalie Wint for their technical guidance and support during the research project and to the ACPOC 2024 organising committee for the opportunity to present the key research outcomes from this work. Lastly thanks to Ayman Al-Kasbi who assisted with the cathodic disbondment and polarisation testing as part of his 3rd year materials engineering research project.

Appendix A. Supplementary data

Supplementary data to this article can be found online at https://doi.org/10.1016/j.porgcoat.2025.109646.

Data availability

The authors do not have permission to share data.

References

[1] J. Elvins, J.A. Spittle, D.A. Worsley, Corros. Sci. 47 (2005) 2740.
[2] I.M. Zin, et al., J. Electrochem. Soc. 148 (2001) B293, https://doi.org/10.1149/1.1381072.
[3] G. Williams, H.N. McMurray, in: B.R.A. Cottis, M. Graham, R. Lindsay, S. Lyon, T.J. (Eds.), Underfilm/Coating Corrosion, 2010.
[4] A. Richardson, D.J.D. Scantlebury, H. Stott (Eds.), Shreir's Corrosion, Elsevier Science, 2009, pp. 988–2004.
[5] I.M. Zin, S.B. Lyon, V.I. Pokhmurskii, M.C. Simmonds, Inhibition of steel and galvanised steel corrosion by zinc and calcium ions in the presence of phosphate, Corros. Eng. Sci. Technol. 39 (2) (2004) 167–173, https://doi.org/10.1179/147842204225016967.
[6] G. Williams, H.N. McMurray, J. Electrochem. Soc. 148 (2001) B377.
[7] S.A. Katz, The Analytical Biochemistry of Chromium by Environmental Health Perspectives 92, 1991, pp. 13–16, https://doi.org/10.1289/ehp.919213.
[8] I. Suzuki, Corrosion Resistant Coatings Technolgy, CRC Pess, 1989.
[9] D. Thierry, D. Persson, G. Luckeneder, K.H. Stellnberger, Atmospheric corrosion of ZnAlMg coated steel during long term atmospheric weathering at different worldwide exposure sites, Corros. Sci. 148 (2019) 338–354, https://doi.org/10.1016/j.corsci.2018.12.033.
[10] J.D. Yoo, P. Volovitch, A.A. Aal, C. Allely, K. Ogle, Corros. Sci. 70 (1) (2013).
[11] P. Volovitch, M. Serdechnova, K. Ogle, Corrosion 68 (2012) 557.
[12] A. Leng, H. Streckel, M. Stratmann, Corros. Sci. 41 (1998) 579.
[13] A. Leng, H. Streckel, M. Stratmann, Corros. Sci. 41 (1998) 547.
[14] A. Leng, H. Streckel, K. Hofmann, M. Stratmann, Corros. Sci. 41 (1998) 599.
[15] E.L. Koehler, J. Electrochem. Soc. 132 (1005) (2006) 5.
[16] S.J. Caraguay, T.S. Pereira, R.O. Giacomelli, A. Cunha, M. Pereira, F.A. Xavier, Surf. Coatings Technol. 437 (2022) 128371.
[17] Y. Yin, H. Zhao, M. Prabhakar, M. Rohwerder, Corros. Sci. 200 (2022) 110252.
[18] W. Fürbeth, M. Stratmann, Corros. Sci. 43 (2001) 229.
[19] C.M. Griffiths, N. Wint, G. Williams, H.N. McMurray, Corros. Sci. 198 (2022) 110111.
[20] P. Ansell, et al., J. Electrochem. Soc. 170 (2023) 011502, https://doi.org/10.1149/1945-7111/aca8d2.
[21] M. Stratmann, R. Feser, A. Leng, Electrochim. Acta 39 (1994) 1207.
[22] J. Sander, L. Kirmaier, M. Manea, D. Shchukin, E. Skordb, Anticorrosive Coatings, Fundamentals and New Concepts, Vincentz Network, Hanover, Germany, 2010, p. 215.
[23] A. Vimalanandan, A. Bashir, M. Rohwerder, Zn-Mg and Zn-Mg-Al alloys for mproved corrosion protection of steel: some new aspects, Mater. Corros. 65 (2014) 392–400, https://doi.org/10.1002/maco.201307586.
[24] A. Bautista, Filiform corrosion in polymer-coated metals, Prog. Org. Coat. 28 (1996) 49–58, https://doi.org/10.1016/0300-9440(95)00555-2.

[25] R.T. Ruggeri, T.R. Beck, An analysis of mass transfer in filiform corrosion, Corrosion-NACE 39 (1983) 452–465, https://doi.org/10.5006/1.3581907.
[26] T.M. Watson, A.J. Coleman, G. Williams, H.N. McMurray, The effect of oxygen partial pressure on the filiform corrosion of organic coated iron, Corros. Sci. 89 (2014) 46–58, https://doi.org/10.1016/j.corsci.2014.08.004.
[27] W.H. Slabaugh, M. Grotheer, Mechanism of filiform corrosion, Ind. Eng. Chem. 46 (1954) 1014–1016, https://doi.org/10.1021/ie50533a053.
[28] G. Williams, H.N. McMurray, The mechanism of group (I) chloride initiated filiform corrosion on iron, Electrochem. Commun. 5 (2003) 871–877, https://doi.org/10.1016/j.elecom.2003.08.008.
[29] W. Schmidt, M. Stratmann, Scanning kelvin probe investigations of filiform corrosion on aluminum alloy 2024-t3, Corros. Sci. 40 (1998) 1441–1443, https://doi.org/10.1016/S0010-938X(98)00044-4.
[30] A. Cristoforetti, S. Rossi, F. Deflorian, M. Fedel, Recent progress in understanding filiform corrosion on organic coated steel: a comprehensive review, Prog. Org. Coat. 192 (2024), https://doi.org/10.1016/j.porgcoat.2024.108469.
[31] N. Wint, D. Eaves, E. Michailidou, A. Bennett, J.R. Searle, G. Williams, H. N. McMurray, The kinetics and mechanism of filiform corrosion occurring on zinc-aluminium-magnesium coated steel, Corros. Sci. 158 (2019) 108073, https://doi.org/10.1016/j.corsci.2019.06.028.
[32] N. Wint, D. Eaves, G. Williams, H.N. McMurray, The use of anion exchange pigments to inhibit the filiform corrosion of zinc-aluminium-magnesium coated steel, Corros. Sci. (2021), https://doi.org/10.1016/j.corsci.2021.109886.
[33] S.J. Mills, A.G. Christy, J.-M.R. Génin, T. Kameda, F. Colombo, Mineral. Mag. 76 (2012) 1289.
[34] N. Van Phuong, K. Lee, D. Chang, M. Kim, S. Lee, S. Moon, Met. Mater. Int. 19 (2013) 273.
[35] A.A. Al-Amiery, W.K. Al-Azzawi, W.N.R.W. Isahak, Isatin schiff as an effective corrosion inhibitor for mild steel in hydrochloric acid solution: gravimetric, lectrochemical and computational investigation, Sci. Rep. 12 (2022) 17773.
[36] R. Talat, M.A. Asghar, I. Tariq, Z. Akhter, F. Liaqat, L. Nadeem, A. Haider, S. Ali, Evaluating the corrosion inhibition efficiency of pyridinium-based cationic surfactants for EN3B mild steel in acidic chloride medias, Coatings 12 (1701) (2022).
[37] H. Nadym, Egypt. J. Pet. 26 (2017) 905–913.
[38] M.A. Amin, O.A. Hazzazi, F. Kandemirli, M. Saracoglu, Inhibition performance and adsorptive behaviou of three amino acids on cold rolled steel in 1.0M HCl-chemical, electrochemical and morphological dtudies, Corr 68 (2012) 688–698.
[39] L. Fan, Y. Gao, Q. Bi, L. Shi, C. Tang, C. Yin, J. Xue, Influence of different anions on the corrosion-inhibition performance of pyridyl ionic liquids, Chem. Pap. 78 (2024) 927–936, https://doi.org/10.1007/s11696-023-03131-5.
[40] Q. Deng, S. Jeschke, B.J. Murdoch, S. Hirth, P. Eiden, J.N. Gorges, P. Keil, X. B. Chen, I. Cole, In-depth insights of inhibitory behaviour of 2-amino-4-methyl-thiazole towards galvanised steel in neutral NaCl solution, Corros. Sci. 199 (2022) 110206.
[41] K. Aramaki, Effects of organic inhibitors on corrosion of zinc in an aerated 0.5 M NaCl solution, Corros. Sci. 43 (2001) 1985–2000.
[42] T. Kosec, D.K. Merl, I. Milosev, Impedance and XPS study of benzotriazole films formed on copper, copper–zinc alloys and zinc in chloride solution, Corros. Sci. 50 (2008) 1987–1997.
[43] A.M. Fenelon, C.B. Breslin, An electrochemical study of the formation of benzotriazole surface films on copper, zinc and a copper-zinc alloy, J. Appl. Electrochem. 31 (2001) 509–516, 47. V. Sirtori, F. Zambon, L. Lombardi, XPS and ellipsometric characterization of zincBTA complex, J. Electron. Mater. 29 (2000) 463–467.
[44] I.A. Kartsonakis, S.G. Stanciu, A.A. Matei, R. Hristu, A. Karantonis, C.A. Charitidis, A comparative study of corrosion inhibitors on hot-dip galvanized steel, Corros. Sci. 112 (2016) 289–307.
[45] S. Deng, M.R. Jeschke, P. Jakeria, S. White, P. Hirth, J.N. Eiden, X.B. Gorges, P. Chen, I. Keil, Cole, Synergistically and sustainably performed inhibitors for galvanised steel against aqueous corrosion, Corros. Sci. 213 (2023) 110984.
[46] N.C. Okey, N.L. Obasi, P.M. Ejikeme, D.T. Ndinteh, P. Ramasami, E.-S. Sherif, E. D. Akpan, E.E. Ebenso, Evaluation of some amino benzoic acid and 4-aminoanti-pyrine derived Schiff bases as corrosion inhibitors for mild steel in acidic medium: synthesis, experimental and computational studies, J. Mol. Liq. 315 (2020) 113773, https://doi.org/10.1016/j.molliq.2020.113773.
[47] S.A. Umoren, U.M. Eduok, Application of carbohydrate polymers as corrosion inhibitors for metal substrates in different media: a review, Carbohydr. Polym. 140 (2016) 314–341, https://doi.org/10.1016/j.carbpol.2015.12.038.
[48] L. Hamadi, S. Mansouri, K. Oulmi, A. Kareche, The use of amino acids as corrosion inhibitors for metals: a review, Egypt. J. Pet. 27 (4) (2018) 1157–1165, https://doi.org/10.1016/j.ejpe.2018.04.004.
[49] D. Kumar, N. Jain, V. Jain, B. Rai, Amino acids as copper corrosion inhibitors: a density functional theory approach, Appl. Surf. Sci. 514 (2020) 145905, https://doi.org/10.1016/j.apsusc.2020.145905.
[50] A. Bazzi, K. Abbiche, S. Izzaouihda, Inhibition efficiency and adsorption mechanism of 4-aminobenzoic acid for copper corrosion in nitric acid medium: a combined experimental and theoretical investigation, Struct. Chem. 32 (2021) 2183–2198, https://doi.org/10.1007/s11224-021-01784-0.
[51] J. Seo, S. Warnke, S. Gewinner, W. Schöllkopf, M.T. Bowers, K. Pagel, G. von Helden, The impact of environment and resonance effects on the site of protonation of aminobenzoic acid derivatives, Phys. Chem. Chem. Phys. 18 (36) (2016) 25474–25482, https://doi.org/10.1039/C6CP04941A.
[52] A. Imjjad, K. Abbiche, M.D. Mellaoui, A. Jmiai, N. El Baraka, A. Ait Taleb, I. Bazzi, S. El Issami, M. Hilali, R. Ben Said, M. Hochlaf, Corrosion inhibition of mild steel by aminobenzoic acid isomers in hydrochloric acid solution: efficiency and adsorption mechanisms, Appl. Surf. Sci. 576 (Part B) (2022), https://doi.org/10.1016/j.apsusc.2021.151780, 151780, ISSN 0169-4332.
[53] T. Eicher, S. Hauptmann, A. Speicher, The Chemistry of Heterocycles, 2003.
[54] O.Ø. Knudsen, A. Forsgren, Corrosion Control through Organic Coatings Boca Raton: A CRC Title, Part of the Taylor & Francis, 2nd (Boca Raton, FL: CRC Press), 2017, p. 276.
[55] O. Gharbi, S. Thomas, C. Smith, N. Birbilis, Npj Mater. Degrad. 2 (2018) 23.
[56] R. Naderi, M.M. Attar, Dyes Pigments 80 (2009) 349.
[57] T.S.N. Sankara Narayanan, Rev. Adv. Mater. Sci. 9 (2005) 130.
[58] G.W.C. Kaye, T.H. Laby, Tables of Physical an Chemical Constants, Longman, London, 1986, p. 219.
[59] N. Wint, N. Cooze, J. Searle, J. Sullivan, G. Williams, H.N. McMurray, G. Luckeneder, C. Riener, The effect of microstructural refinement on the localized corrosion of model Zn-Al-Mg alloy coatings on steel, J. Electrochem. Soc. 166 (11) (2019) C3147–C3158, https://doi.org/10.1149/2.0171911jes.
[60] G. Williams, A.J. Coleman, H.N. McMurray, Inhibition of aluminium alloy AA2024-T3 pitting corrosion by copper complexing compounds, Electrochim. Acta 55 (20) (2010) 5947–5958. ISSN 0013-4686, https://doi.org/10.1016/j.electacta.2010.05.049.
[61] G. Williams, H.N. McMurray, S.M. Powell, D.A. Worsley, Electrochim. Acta 45 (2008) 2165.
[62] D.A. Worsley, H.N. McMurray, J.H. Sullivan, I.P. Williams, Corrosion 60 (2004) 437.
[63] N. Khayatan, J. Manoj Prabhakar, E. Jalilian, N. Madelat, H. Terryn, M. Rohwerder, On the rate determining step of cathodic delamination of delamination-resistant organic coatings, Corros. Sci. 239 (2024) 112396. ISSN 0010, https://doi.org/10.1016/j.corsci.2024.112396.
[64] N. Khayatan, M. Rohwerder, A new insight into the rate determining step of cathodic delamination, Corros. Sci. 202 (2022), https://doi.org/10.1016/j.corsci.2022.110311.
[65] H. Leidheiser Jr., Corrosion 38 (1982) 374.
[66] H. Leidheiser, W. Wang, L. Igetoft, Prog. Org. Coat. 11 (1983) 19.
[67] Xu Min, C.N. Catherine Lam, Dennis Wong, Edouard Asselin, Evaluation of the cathodic disbondment resistance of pipeline coatings – a review, Prog. Org. Coat. 146 (2020).
[68] N. Wint, P. Ansell, J. Edy, G. Williams, H.N. McMurray, J. Electrochem. Soc. 166 (2019) C580.
[69] H.N. McMurray, G. Williams, Ref. Modul. Mater. Sci. Mater. Eng. 1 (1) (2016).
[70] M.-W. Huang, C. Allely, K. Ogle, M.E. Orazem, J. Electrochem. Soc. 155 (2008) C279.
[71] W. Fürbeth, M. Stratmann, Corros. Sci. 43 (2002) 229.
[72] G. Williams, P. Morgan, Meet. Abstr. (2023), https://doi.org/10.1149/MA2023-02131118mtgabs. MA2023-02 1118.
[73] D. Filotás, J. Izquierdo, B.M. Fernández-Pérez, L. Nagy, G. Nagy, R.M. Souto, Contributions of microelectrochemical scanning techniques for the efficient detection of localized corrosion processes at the cut edges of polymer-coated galvanized steel, Molecules 27 (7) (2022 Mar 27) 2167, https://doi.org/10.3390/molecules27072167. PMID: 35408563; PMCID: PMC9000633.
[74] A.C. Bastos, et al., J. Electrochem. Soc. 164 (2017) C973.
[75] J. Sullivan, N. Cooze, C. Gallagher, T. Lewis, T. Prosek, D. Thierry, In situ monitoring of corrosion mechanisms and phosphate inhibitor surface deposition during corrosion of zinc-magnesium-aluminium (ZMA) alloys using novel time-lapse microscopy, Faraday Discuss. 180 (2015) 361–379, https://doi.org/10.1039/c4fd00251b.
[76] A. Bazzi, K. Abbiche, S. Izzaouihda, et al., Inhibition efficiency and adsorption mechanism of 4-aminobenzoic acid for copper corrosion in nitric acid medium: a combined experimental and theoretical investigation, Struct. Chem. 32 (2021) 2183–2198, https://doi.org/10.1007/s11224-021-01784-0.
[77] D.R. Lide (Ed.), CRC Handbook of Chemistry and Physics, 87th ed., CRC Press, 2006.
[78] L.G. Sillen, A.E. Martell, Stability Constants of Metal-Ion Complexes, The Chemical Society, London, 1964.
[79] L. Haiqing, J. Muhammad, Z. Jingmao, F. Baomin, T. Mohammad, M. Muhammad, M. Mubashar, W. Jingbao, Filiform corrosion inhibition of Zn–Al–Mg-coated steel by Ti–Zr conversion coating: crucial role of benzotriazole-5-carboxylic acid, Am. Chem. Soc. (2025), https://doi.org/10.1021/acs.langmuir.5c00791.